frontiers | Frontiers in Earth Science

TYPE Original Research
PUBLISHED 21 April 2023
DOI 10.3389/feart.2023.1186901

OPEN ACCESS

EDITED BY
Xiaoming Shen,
Ministry of Emergency Management, China

REVIEWED BY
Gaoyuan Sun,
Hohai University, China
Hanwen Dong,
Chinese Academy of Geological Sciences (CAGS), China

*CORRESPONDENCE
Zhongpeng Han,
hanzp@cugb.edu.cn

RECEIVED 15 March 2023
ACCEPTED 10 April 2023
PUBLISHED 21 April 2023

CITATION
Ma Z, Han Z, Li Y, Xu T, Han X, Bi W and Zhang W (2023), Late Cenozoic cooling and evolution history of the Kangmar dome in southern Tibet: Insights from inverse thermal modeling.
Front. Earth Sci. 11:1186901.
doi: 10.3389/feart.2023.1186901

Late Cenozoic cooling and evolution history of the Kangmar dome in southern Tibet: Insights from inverse thermal modeling

Zining Ma[1], Zhongpeng Han[2]*, Yalin Li[1], Tiankun Xu[1], Xu Han[1], Wenjun Bi[3] and Wenzhong Zhang[1]

[1]School of Earth Sciences and Resources, China University of Geosciences, Beijing, China, [2]Institute of Earth Sciences, China University of Geosciences, Beijing, China, [3]Department of Earth Sciences and Engineering, Taiyuan University of Technology, Taiyuan, China

The North Himalayan Gneiss Domes, which are essential parts of the Cenozoic extensional structures in Southern Tibet, record the thermal and tectonic processes that occurred after the India-Asian collision and are thought to be effective structures regulating post-collision intracontinental deformation. However, it is still unclear how these domes are formed and how they contribute to the regulation process. Here, we performed detailed geological mapping, elevation transect sampling, low-temperature thermochronological testing, and 3D modeling on the Kangmar dome, which is located west of the N–S treading Yadong-Gulu rift, and its core-cover contact fault is suspected to be the northern continuation of the South Tibetan Detachment System (STDS). Our analysis revealed a discrepancy in the deformation histories of the dome's northern and southern portions. We proposed a model in which the core-cover contact fault of the Kangmar dome was a part of the South Tibetan Detachment System and the doming event that occurred at ~12.2 Ma was dominated by thrust stacking of the southward mid-crustal channel flow. The rapid cooling following the middle Miocene was possibly influenced by the N–S Trending Yadong-Gulu rift activity. The present landscape was shaped by the incision of the Nianchu River, which was accompanied by increased glacial activity during the Pleistocene. Our findings enhance the intracontinental deformation patterns following collisions and shed light on the numerous domes in Himalayas and other orogenic belts.

KEYWORDS

southern Tibet, exhumation, low-temperature thermochronology, Pecube, Kangmar dome

1 Introduction

The North Himalayan Gneiss Domes (NHGDs) are ubiquitous structures within the Himalaya orogen belt, which, together with the N–S trending normal faults and the Southern Tibetan detachment systems, compose the typical postcollision extensional structures in northern Himalaya (Zhang et al., 2012). These well-exposed middle-lower crustal rocks are archives of the crustal thickening, metamorphism, melting, deformation, and exhumation processes that occurred throughout the convergence of India and Eurasia (e.g., Schärer et al., 1986; Lee et al., 2000; Lee et al., 2006; Quigley et al., 2008; Zeng et al., 2009; Gao and Zeng., 2014). Various formation mechanisms and the geological evolution of the domes have been

hypothesized (Le Fort et al., 1987; Chen et al., 1990; Lee et al., 2000; Larson et al., 2010). Particular domes have been studied via limited research methods, the evolutionary history of gneiss domes has been intensely debated. This has also led to a lack of clarity regarding the interconnection of Cenozoic extensional structures in southern Tibet.

Eskola (1949) initially stated that a mantled gneiss dome was composed of a metamorphic-plutonic complex core that was overlain by supracrustal strata. After the discovery of extensional detachment faults (Coney et al., 1980), a number of classic gneiss domes (e.g., Simplon metamorphic terrane in the Alps; gneiss domes in the Variscan belt) have been construed as extensional metamorphic core complexes (Mattauer et al., 1988; Mancktelow and Pavlis., 1994; Wawrzyniec et al., 2001). The high-strain detachment faults of gneiss dome systems usually form core-cover contact faults, which separate the dome cores from their overlying strata (Jessup et al., 2019). The difference in perception of the core-cover contact fault is also reflected in a controversy over the last few decades regarding the formation mechanisms of the typical gneiss domes found throughout the globe, which has led to three main mechanisms: 1) diapirism (Ramberg, 1980), 2) crustal shortening (e.g., Brun, 2003; Ramsay, 1967), and 3) crustal extension (e.g., Miller et al., 1992). Jessup et al. (2019) classified the kinematic models that were derived from these mechanisms and applied to the NHGD into three inconsistent groups: 1) diapirism and/or buoyancy-driven models (e.g., Le Fort et al., 1987); 2) metamorphic core complex models (e.g., Chen et al., 1990); and 3) out-of-sequence thrusting and/or folding models (Lee et al., 2000; Larson et al., 2010). Predictably, apart from the activity of the core-cover contact fault, which to some extent influences the exhumation history of the dome, it is conceivable that the precise definition of the kinematic property, activity processes, and affiliation of the dome plays a decisive part in exploring the domes' formation mechanism and geotectonic evolution.

Although the gneiss core and overlying strata of the Kangmar dome have been dated sufficiently by prior studies (Debon, 1980; Xu and Jin, 1986; Liu et al., 2004; Wang et al., 2018), the spatiotemporal evolution history has not been elucidated. As a distinct extensional structure, the exhumation of the gneiss core and the timing and intensity of the detachment fault are crucial for understanding the doming process, which remains ambiguous. This study aims to address the cooling histories between the southern and northern portions of the dome through detailed geochronological investigations and via the thermochronological dating of samples collected along elevation transects. We apply multiple-scenario thermokinematic modeling to clarify the evolutionary history of the core-cover contact fault, the rock uplift, and the river incision that occurred following the doming event to create a bridge between dome formation and regional structural activities. Coupled with the morphological analyses of the Nianchu River and the explanation of the rapid cooling events, we shed additional light on how the Kangmar dome formed and was exhumed. Our results suggest that the hanging wall of the core-cover contact fault has an overall northward movement, and the doming event occurred first in its southern portion ~12.2 Ma, which was much earlier than that in the northern portion. The second rapid cooling in the Pleistocene was mainly due to glaciation intensified by global cooling.

2 Geological background

2.1 Regional geological setting

The Himalayan orogenic belt was formed by the continuous convergence of the Indian and Eurasian continents after their initial collision during the early Cenozoic (Molnar and Tapponnier, 1975; Yin and Harrison, 2000; Li et al., 2012; Meng et al., 2012). Crustal shortening and extension are two deformational styles in the Himalayan orogenic belt (Li et al., 2015), forming the thrust structures of the Main Frontal Thrust (MFT), the Main Boundary Thrust (MBT), and the Main Central Thrust (MCT) from the south and the extensional South Tibetan Detachment System (STDS) to the north. These structures divide the Himalayan orogenic belt into four parts from south to north: the Sub-Himalayan Sequence (SHS), the Lesser Himalayan Sequence (LHS), the Greater Himalayan Crystalline Complex (GHC) and the Tethyan Himalayan Sequence (THS) (Figure 1A).

The Tethys Himalayan Sequence is bounded by the Indus-Yarlung suture zone (IYTZ) to the north and the STDS to the south, which represent the remnants of the stratigraphic sequence deposited along the India passive margin toward the Neotethys Ocean (Sciunnach and Garzanti, 2012). This area is separated into southern and northern sections by the Gyirong-Kangmar thrust (GKT) (Ratschbacher et al., 1994). The N–S Trending Rifts (NSTR) (Figure 2A) and NHGD are located within these sedimentary strata and, together with the STDS, form a typical postcollisional extensional structure in the northern Himalayas. The NHGD is exposed within the THS (Figure 1A). It consists of more than ten discontinuous, subparallel latitudinal band-spreading domes, including from west to east the Malashan, Lhagoi Kangri, Mabja, Kampa, Kangmar, Ramba, Yardoi, and Cuonadong gneiss domes (e.g., Zhang et al., 2004; Aikman et al., 2008; King et al., 2011; Zeng et al., 2011; Liu et al., 2014). With an average peak elevation of over 5,000 m, the dome belt trail is consistent with the partial drainage divide of the Yarlung Tsangpo River (Figure 1B).

Numerous previous studies on leucogranite rocks within the NHGD have documented a series of crystallization and emplacement ages ranging from 47 to 7 Ma (e.g., Lee et al., 2004; Zeng et al., 2011; Gao et al., 2012; Liu et al., 2014; Ji et al., 2020; Chen et al., 2022) and cooling ages that range from 22 to 6 Ma (e.g., Lee et al., 2000; Lee et al., 2004; Guo et al., 2008). With deformation and metamorphic characteristics almost identical to the GHS, it was proposed that the NHGD domes were part of a laterally continuous plane with the GHS at the onset of Himalayan orogenesis (Harrison et al., 1997; Beaumont et al., 2001; Beaumont et al., 2004; Lee et al., 2006; Ding et al., 2016), and combined with the fact that the cores of these domes are always subducted beneath the THS, their core-cover contact faults are therefore widely recognized as continuous parts of the STDS (Chen et al., 1990; Hauck et al., 1998; Liu et al., 2014). The current research consensus on elevation histories is that two major ductile deformation events were recorded in those domes: an older N–S shortening and vertical thickening episode and a younger N–S extensional and vertical thinning episode, which were bracketed in age between late Eocene-early Oligocene to middle Miocene (Chen, 1997; Lee et al., 2000; Zhang et al., 2004; Aoya et al., 2005; Aoya et al., 2006; Quigley et al., 2006; Kawakami et al., 2007; Quigley et al., 2008).

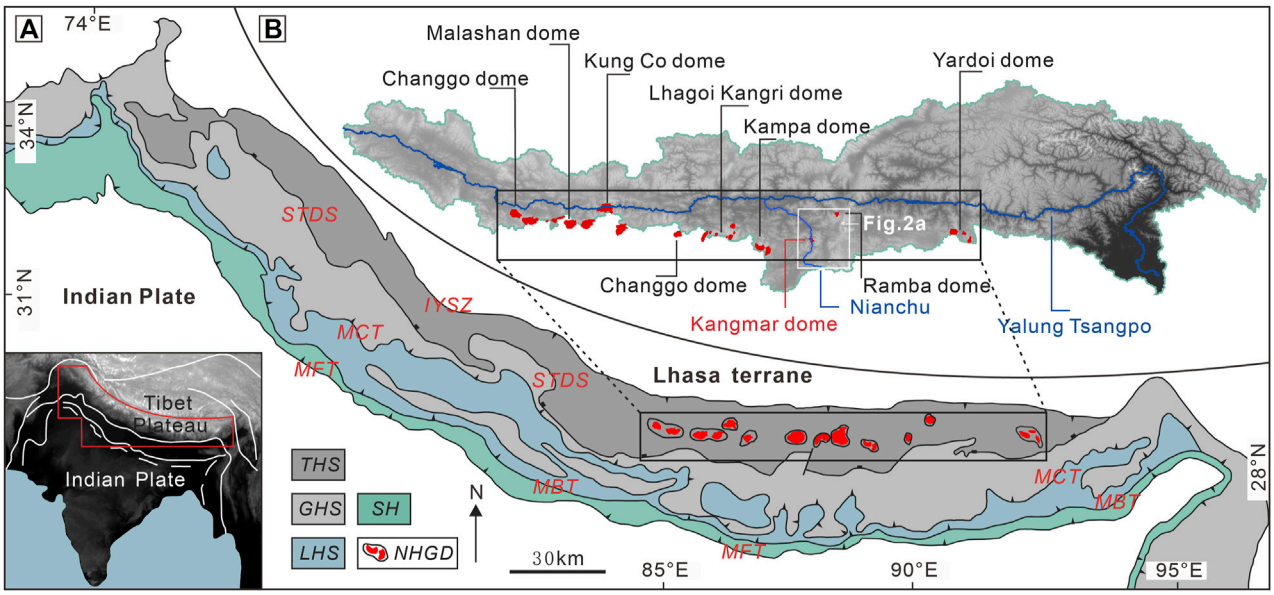

FIGURE 1
(A) Simplified geologic map of the Himalayan orogenic belt, southern Tibet, showing locations of the North Himalayan Gneiss Dome (modified after Wang et al., 2022). **(B)** Simplified geologic map of the Yarlung Tsangpo catchment, showing the relative locations of the NGHD, Nianchu River and Yalung Tsangpo River. MBT, Main Boundary thrust; MCT, Main Central thrust; MFT, Main Frontal thrust; STDS, South Tibetan detachment system; IYSZ, Indus-Yarlung suture zone; THS, Tethys Himalaya Sequence; GHS, Grater Himalaya sequence; LHS, lesser Himalaya sequence; SH, sub-Himalaya; NHGD, North Himalayan Gneiss Dome.

Topographically, the Yarlung Tsangpo catchment and the Ganges catchment area are bordered in southern Tibet, and their dividing line roughly coincides with the NHGD uplift belt (Figure 1B), to the south of which most of the rivers drain southward into the Ganges, except the Nianchu River. As one of the largest tributaries of the Yarlung Tsangpo, the Nianchu River originates from the Greater Himalaya (Chongbayong Co., 28.22°N, 89.64°E, 4,575 m above sea level) and drains the THS with a total length of 190 km (Figure 2A). The Kangmar dome is deeply incised by the Nianchu River, which preserves the high-steepness of the stream-valley landscape.

2.2 Geology of the Kangmar dome

The Kangmar dome (Figure 3A), located in the eastern segment of the NHGD, contains a gneiss core that is mantled by Precambrian basement metasedimentary rocks and overlain by the low-grade metamorphic to non-metamorphic THS. The core-cover contact fault is fully exposed in the stream valley formed by the Nianchu River and is characterized as a low-angle ductile shear belt (Figure 3A). Above the contact is the hanging wall unit, which is composed of Ordovician to Cretaceous rocks that range from metamorphosed schist rocks at the base to unmetamorphosed sedimentary rocks at the top. Apart from the valley landscape, there are several glacial relics represented by glacial valleys (Figure 3B), resulting in the intermittent presence of tributaries of the Nianchu River.

Additional U–Pb dating of the gneiss core has revealed crystallization ages of 520–478 Ma (Schärer et al., 1986; Lee et al., 2000; Xia et al., 2008; Gao et al., 2019). A combination of $^{40}Ar/^{39}Ar$ thermochronology ages obtained from the core or from the ductile shear belt has shown two phases of cooling for the Kangmar dome at ~20 and ~13 Ma (Chen., 1979; Lee et al., 2000; Liu et al., 2004; Wang et al., 2015). These cooling ages were interpreted as partial thermal events or responses to fault activity. There is a general trend of younger values from south to north (Figure 3C).

3 Approach and methods

3.1 Geological mapping and sample processing

The outcropping of strata in the Kangmar dome and adjacent regions resulted in widespread exposure of typical internal structures, which are ideal features to explore the deformation characteristics of the dome. The geological mapping of the Kangmar dome includes measurements of stretching lineations preserved within the gneiss core and observations of the complex deformation structures within the core-cover contact fault shear zone and cover strata. Compared to the abundant thermochronology results from samples distributed from the incoming horizontal elevation (e.g., Chen., 1979; Lee et al., 2000; Liu et al., 2016; Wang et al., 2015), there are few data points from the age-elevation transects that could be used to calculate exhumation rates, assuming temporally and spatially invariant horizontal isotherms (Wagner and Reimer, 1972). To understand the evolution history, we collected samples from two

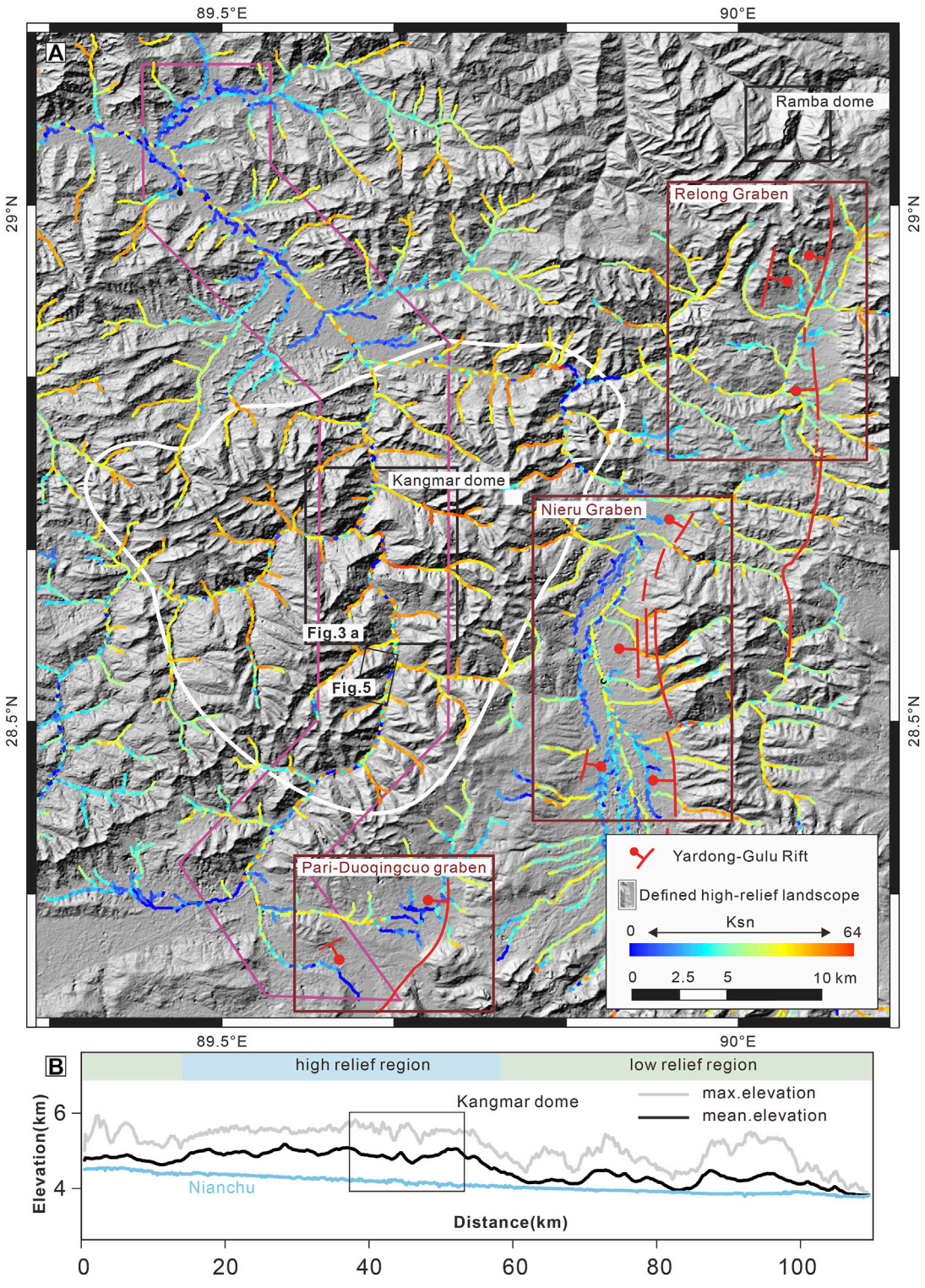

FIGURE 2
(A) Regional channel steepness in parts of the Nianchu catchment. See Figure 1 for location. Two black boxes mark the locations of the Kangmar and Ramba domes. The dark red frames mark the regional segments of the Yadong-Gulu rift. **(B)** Swath profile [corresponding to the purple rectangular box in **(A)**] along the Nianchu River, showing the undulating topography along the Nianchu River.

subvertical transects along two ridges on the gneiss core, located in the northern and southern portions of the dome (Figure 3A). The two transects were sampled over a relief of ~720 m (southern transect) and ~860 m (northern transect) along the ranges and both within a limited horizontal distance. The rocks sampled are all gneiss with a sampling interval of ~100 m.

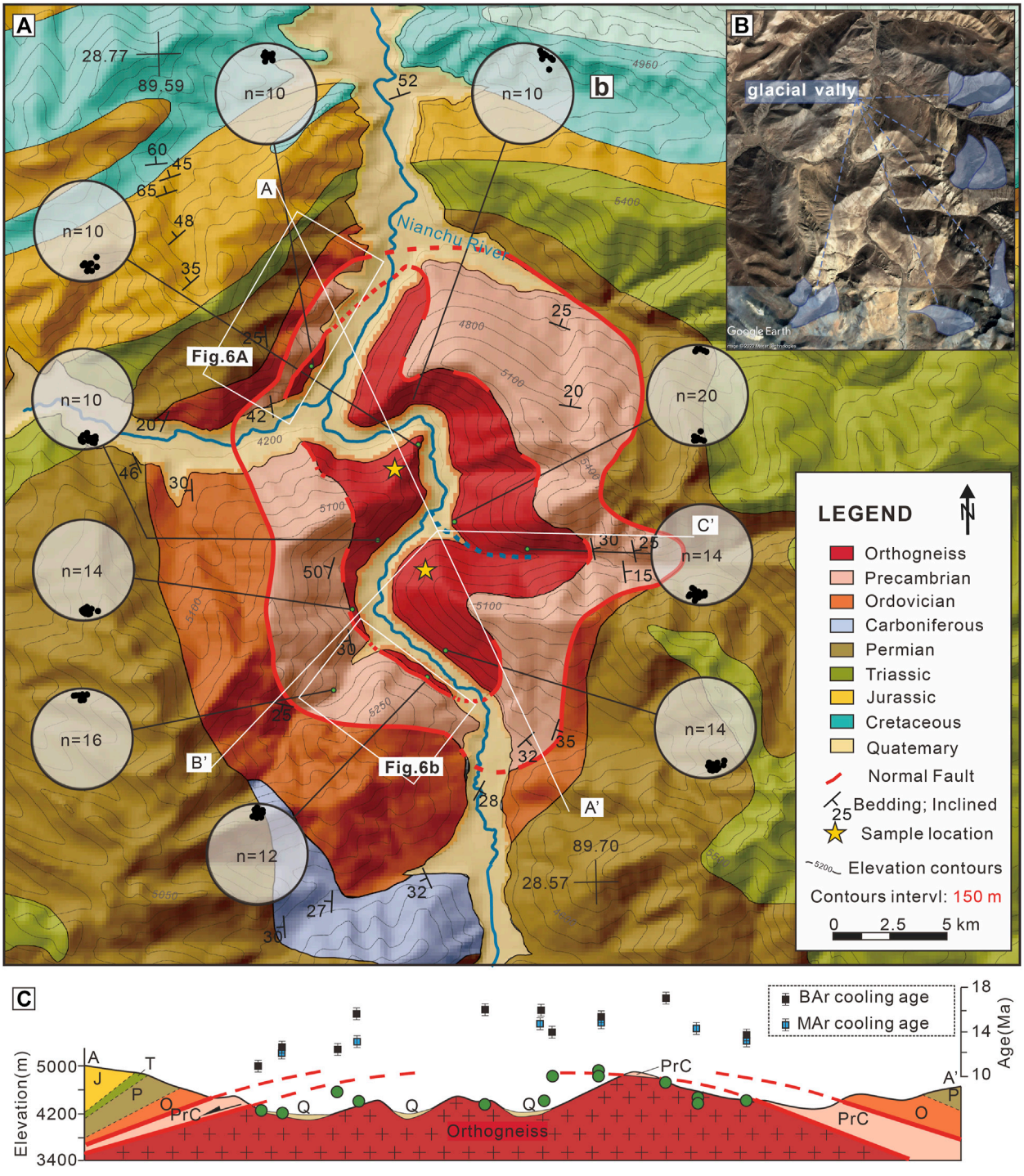

FIGURE 3
(A) Simplified geologic map of the Kangmar gneiss dome. **(B)** Satellite image of the Kangmar dome area, marking the glacial remains represented by the ice erosion valley. **(C)** Composite structure-age diagram of the Kangmar dome. The locations of cross-section lines are shown in **(A)**, and ages are cited from Lee et al. (2000) and show an increasing trend from south to north.

3.2 Low-temperature thermochronology

Low-temperature thermochronometry is a technique that reconstructs the thermal evolution of the upper crust (<5 km) (Wagner and Van den Haute, 2012) for examining the cooling history of footwall samples exhumed via normal fault exhumation mechanisms that include time-varying rock uplift and landscape evolution (Reiners and Shuster, 2009; Ault et al., 2019). We use apatite fission track (AFT), zircon (U-Th)/He (ZHe) and zircon fission track (ZFT) dating for this study, which covers a large scale of

TABLE 1 Summary of new AFT, ZHe, and ZFT data reported in this study.

Sample no.	Ele. (m)	Lat. (N°)	Long. (E°)	AFT age (Ma) (±1σ)	MTL (μm)/N	ZHe age (Ma) (±1σ)	ZFT age (Ma) (±1σ)
Southern transect							
D0812	5,100	28.6416	89.6688	5.9 ± 0.9	10.98/5	9.2 ± 0.5	15.0 ± 0.7
D0813	5,000	28.6439	89.6653	5.4 ± 0.9			
D0814	4,900	28.6461	89.6631	4.3 ± 0.7			
D0815	4,800	28.6485	89.6624	3.5 ± 0.5			
D0816	4,700	28.6502	89.6623	4.5 ± 0.7		9.2 ± 0.6	13.6 ± 0.6
D0817	4,620	28.6516	89.6618	2.7 ± 0.5			
D0819	4,460	28.6545	89.6613	3.7 ± 0.5			
D0820	4,380	28.6563	89.6614	4.6 ± 0.6	13.40/12	8.7 ± 0.6	17.3 ± 0.9
Nouthern transect							
D7101	5,060	28.6650	89.6437	8.9 ± 3.9			
D7103	4,860	28.6670	89.6486	5.9 ± 0.7	11.07/16	9.2 ± 0.5	14.7 ± 0.6
D7105	4,660	28.6730	89.6531	6.0 ± 0.7	12.26/40	8.9 ± 0.6	16.8 ± 0.8
D7107	4,420	28.6809	89.6577	5.8 ± 0.8	11.50/47		
D7108	4,310	28.6825	89.6587	4.1 ± 0.7	11.76/50		
D7109	4,200	28.6846	89.6597	2.7 ± 0.5		9.2 ± 0.5	

annealing and retention and ranges from ambient temperatures to ~190°C (Reiners, 2005; Ketcham et al., 2007; Tamer and Ketcham, 2020). Here, we present 14 AFT, 6 ZHe, and 5 ZFT samples (Table 1).

AFT and ZFT analyses for the two transects were performed at Apatite Technology Co., Ltd., whereas ZHe analyses were performed at The University of Melbourne. Details of the experimental procedure are in Supplementary Text S1.

3.3 Morphometry analysis of the Nianchu River

The morphological study of the rivers in the region is also included in our work, as we assume that a precise sequencing of fluvial formation and tectonic activity are essential prerequisites for a rational exploration of cooling history. The bedrock channel response to differential rock uplift could be measured by the channel-steepness index k_{sn} (Whipple and Tucker, 1999; Kirby et al., 2003), which is based on the power-law relationship: $S = k_s A^{-\theta}$ (S: local channel slope; A: contributing drainage area; θ: concavity index; Flint, 1974). We adopted the principle to measure the local channel slope (S) for the change in upstream drainage area (A) along the length of the channel profiles and then calculated a normalized channel steepness (k_{sn}) using a fixed reference concavity $\theta = 0.45$, as shown by Liang et al. (2020). Channel steepness values are color coded for the river channels shown in Figure 2A to highlight the changes in channel morphology along with their channel profiles. A high-relief landscape area was also defined that encompassed the region in which the main channel or tributaries of the Nianchu River had relatively high K_{sn} values. The distribution of N–S trending Yadong-Gulu rifts was also superimposed to visually represent the possible response of the river to fault activity.

4 Results

4.1 Deformation characteristics of the dome

The gneiss core contains a well-developed stretching lineation, which is defined by aligned biotites and weakly flattened quartz grains (Figure 4B). Measurements of stretching lineations were spread over the entire gneiss core and resulted in an approximately N–S treading (Figure 3A). Meanwhile, mesostructures observed within the ductile shear belt of the core-cover-contact fault show a nearly identical kinematic stress direction of N–S (Figure 4E). The kinematic stress structures observed over the contact began to exhibit an additional progressively more pronounced E–W extension, composed of K-feldspar porphyroblasts to S-C fabric (Figures 4C, D), which indicates E–W shearing in direction and magnitude with the gneiss core. The lower Permian slate layer (Figure 5A), located in the southern position of the covering low-grade metamorphic rock, retains large-scale shear-type boudinage structures (Figure 5B), indicating vertical thinning due to top-to-the-N shearing. The kink band (Figure 5C) superposed on preexisting asymmetrical folds also shows top-to-the-N shearing.

The circular shape indicating the exposed core-cover contact fault was recognized as a normal fault on both the southern and

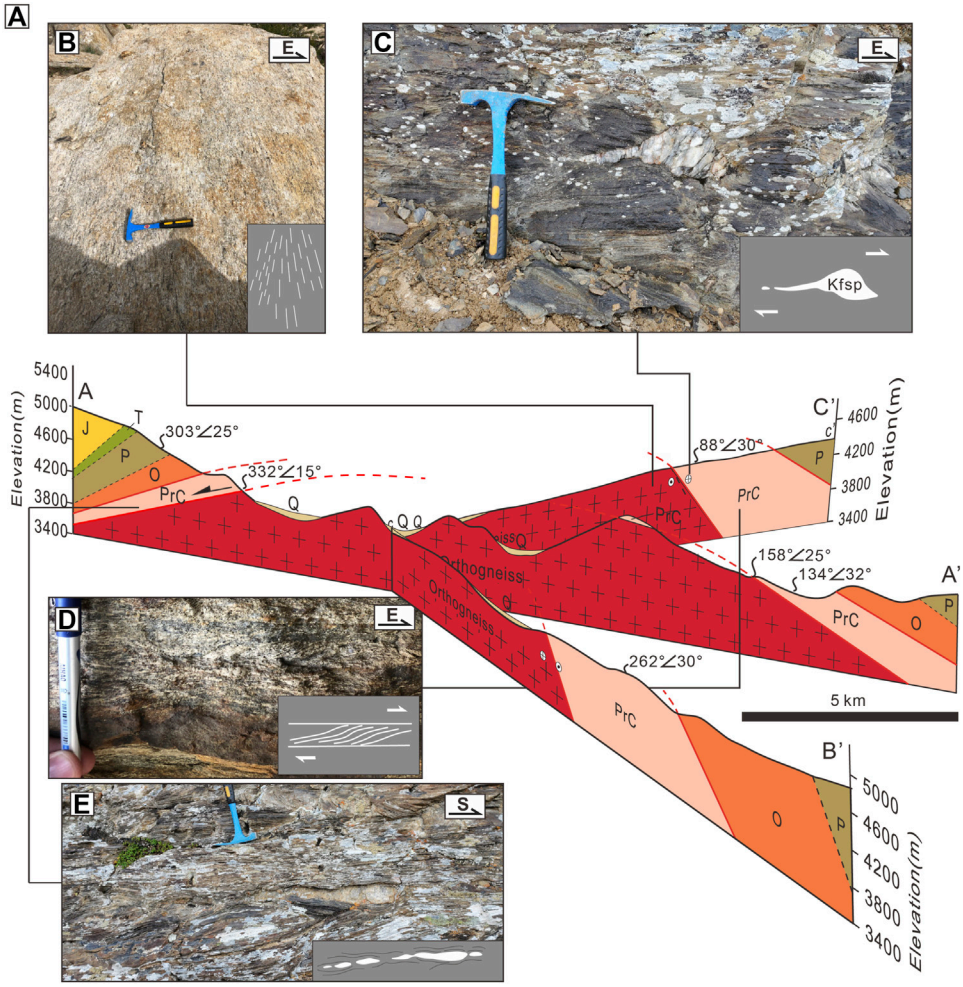

FIGURE 4
(A) Composite diagram illustrating the three-dimensional structure of the Kangmar dome. The locations of the cross-section lines and legend are shown in Figure 3A. **(B–E)**: Summary of kinematic structures in different positions of the Kangmar dome.

northern portions of the dome (Figure 6). The dip of the core-cover contact fault differs and the southern part shows a greater inclination (25°) than the northern portion (15°) (Figure 4A). The cover of both dome portions is consistent in terms of lithological succession but differs in thickness, with the southern portion displaying significantly thicker than the northern portion. This is especially the case in the Precambrian crystallization basement, which shows an apparent thickness of ~620 m in the southern portion (Figure 6A) and only ~380 m in the northern portion (Figure 6B).

4.2 Low-temperature thermochronology ages

The AFT ages of fourteen gneiss samples range from 2.7 ± 0.5 to 8.9 ± 3.9 Ma (Tables 1, 2). The Southern transect ages range from 2.7 to 5.9 Ma, whereas the northern transect ages range from 2.7 to 8.9 Ma (Table 2). The AFT dating of the southern transect included eight samples, all of which passed the $\chi 2$ test, representing a single age population (Galbraith and Laslett, 1993), which suggests that these samples experienced full annealing for their AFT ages. The AFT dating of the northern transect included six samples. Samples D0701, D0707, and D0708 yield AFT ages of 8.9 ± 3.9, 5.8 ± 0.8 and 4.1 ± 0.7 Ma, respectively (Supplementary Figure S1), which did not pass the $\chi 2$ tests, suggesting multiple age populations (Galbraith and Laslett, 1993). The two transects both show clear age-elevation relationships (Figures 7D, E). Six samples (D0812, D0820, D0703, D0705, D0707, and D0708) from the two transects have relatively consistent and short unprojected mean horizontal confined track lengths, with negative skewness (Supplementary Figure S1; Table 2), which range from 10.98 to 13.40 μm. This suggests that these samples had a relatively short stay at the partial annealing zone and represent metamorphic rocks that cooled fast as they neared the surface (Wang et al., 2018; Bi et al., 2022).

Twenty-two single-grain ZHe dates from six samples have been reported (Table 3). Generally, the ZHe ages offer a narrow range of ~9 Ma. For the two transects, the ages of samples are mostly reproducible, and the plots of the ZHe ages versus grain size or effective Uranium [(eU) = (U) + 0.235 × (Th)] content show no clear

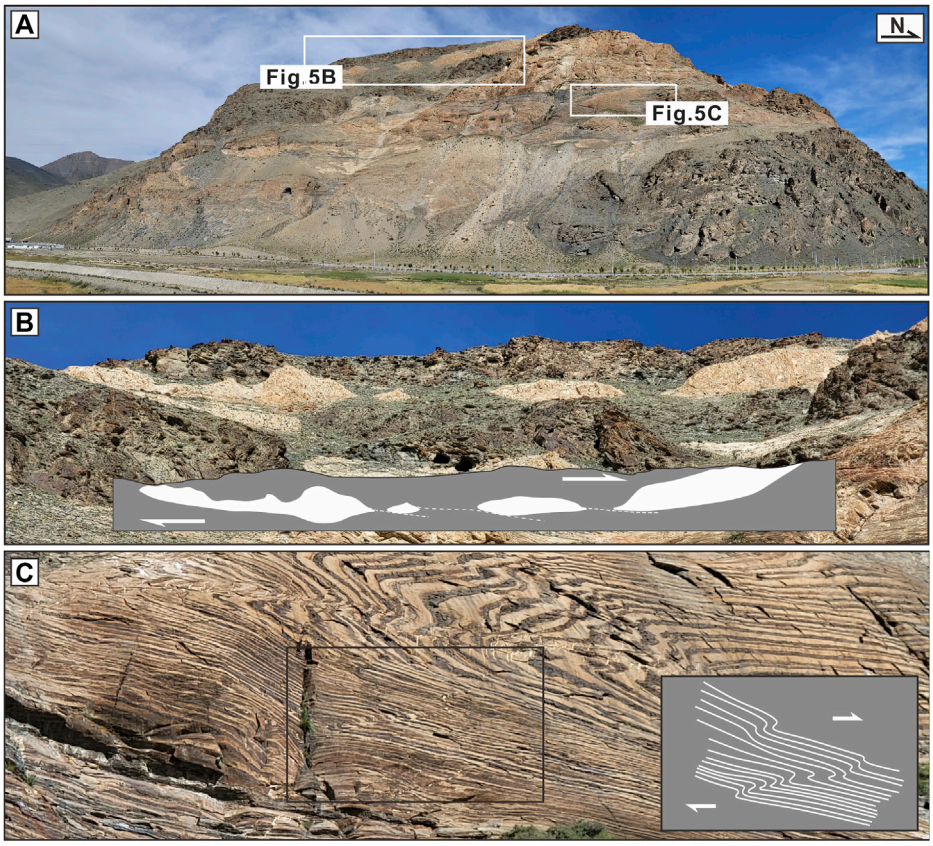

FIGURE 5
(A) Structural observation within the lower Permian slate layer, **(B)** large-scale shear-type boudinage representing near top-to-the-N shearing and vertical thinning, and kink band structure **(C)** in the structural lower level representing the northward movement of the upper strata.

relationship (Supplementary Figure S2); hence, radiation damage does not appear to influence the age distribution (Guenthner et al., 2013).

The ZFT ages of the five gneiss samples range from 14.7 ± 0.6 to 17.3 ± 0.9 Ma (Tables 1, 4). All samples failed to pass the $\chi 2$ test (Supplementary Figure S3), perhaps because of the poor quality of zircons; therefore, the central zircon fission track ages were preferred, which ranged from 13.6 ± 0.6 to 17.3 ± 0.9 Ma in the southern transect and 14.7 ± 0.6 to 16.8 ± 0.8 Ma in the northern transect. Neither of the two transects had enough confined track lengths to determine their cooling modes.

All the low-temperature thermochronology ages are younger than their corresponding zircon U–Pb ages of 520–478 Ma (Schärer et al., 1986; Lee et al., 2000; Xia et al., 2008; Gao et al., 2019), suggesting that these ages were generated by monotonic cooling after magma emplacement and crystallization (Gleadow et al., 1986).

4.3 Channel steepness index of the Nianchu River

The morphology of the Nianchu drainage is generally inhomogeneous, even though the channel steepness of the Nianchu mainstream remains within a limited range for the majority of stream segments. Its tributaries in the upper and lower reaches have similar Ksn values of <40, which were smaller than those in the middle reaches (40-64) within the Kangmar dome region. Although some tributaries were not identified in our fieldwork, these tributaries identified by GIS within the Kangmar dome area could perhaps be regarded as intermittent rivers, and their ksn values can also be used to characterize the steepness of the river valley in this region. These rivers with high ksn values (>40) are circled by the white line in Figure 2A and represent high-relief geomorphology, which suggests that the Nianchu River has undergone a low-relief to high-relief landscape transition during its upper-middle reaches and trends toward a low-relief landscape in its middle-lower reaches. The Kangmar dome is basically located in the center of the defined high-relief landscape area.

5 Thermokinematic modeling (Pecube)

The Pecube modeling process considers landscape evolution (topography, relief), the crustal thermal regime, tectonic setting (fault configurations, surface uplift or subsidence) and the isostasy to quantify thermal histories for rock particles at depth during exhumation or burial contexts (Braun, 2003; Braun et al., 2012). The Pecube thermokinematic program allows the testing of

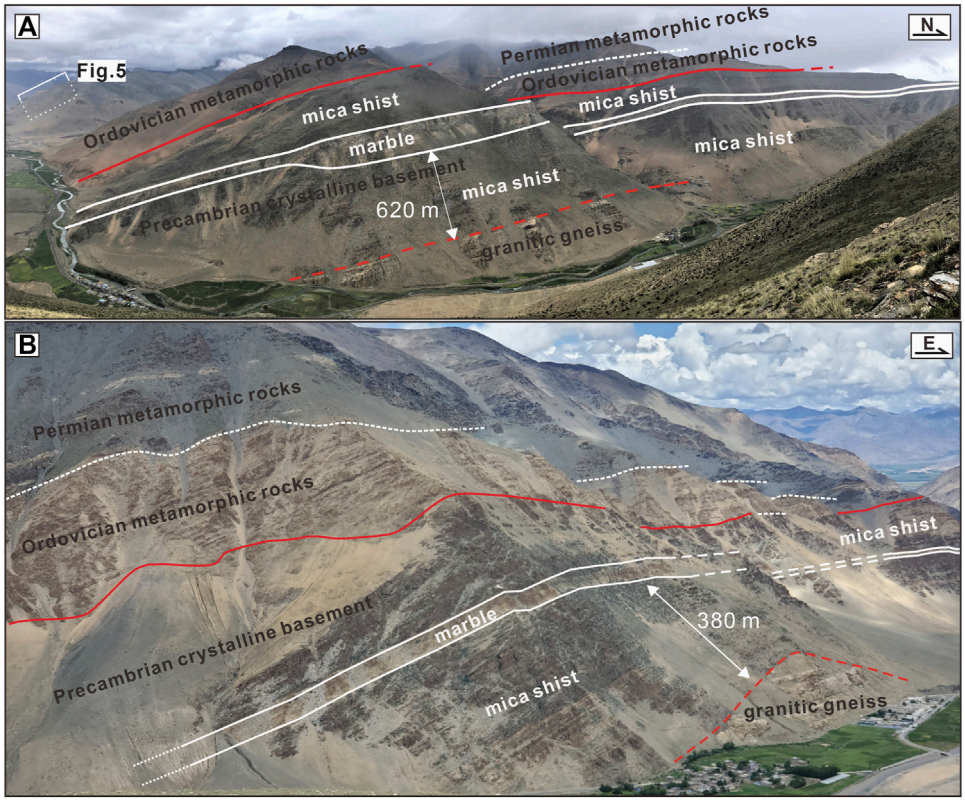

FIGURE 6
Field relationships in the Kangmar dome. **(A)** East-looking view of the south portion, and **(B)** south-looking view of the north portion. Photographs taken from the location and orientation indicated by white boxes in Figure 3 show that the strata sequence was continuous, but the distance between the "core-cover contact" and marker-bed marble belt in the Precambrian basement was significantly different.

multiple tectonic scenarios and predicts the geographic distribution of thermochronological ages for individual samples. As part of this process, it solves the 3D heat equation in the crust and takes into account exhumation through lateral and vertical rock kinetics, as well as relief evolution. By reducing the misfit function between predictions and observations, we employed Pecube v3.0 (Braun et al., 2012) in inverse modes (neighborhood algorithm; Sambridge, 1999a; Sambridge, 1999b) to establish optimal value ranges for the tested parameters.

5.1 Model setup

In the Pecube modeling, geological scenarios accommodate temporal fluctuations in vertical exhumation rates and fault slip rates, either separately or in combination. Exhumation or topographic changes between different phases can be defined by different transition times (Ou et al., 2021). We defined an "exhumation scenario" that considers exclusively vertical exhumation rates that change geographically and temporally to maintain the present topography over time. Our new AFT ages are similar in age results to Lee et al. (2000) but show an opposite increase in the trends of different ages within the same tectonic layer (Figures 3C, 7D, E). Coupled with the difference in geological observations and dating ages between the southern and northern transects of the Kangmar dome, it is reasonable to propose that the two portions have different cooling rates; therefore, we modeled the two portions separately in the "exhumation scenario" (Supplementary Table S2). Models were started at 20 Ma to encompass the history recorded by most of our measured data. We have divided the timeline into many phases to give maximum freedom to the free parameters in the inversion. These resulting transition times are not geologically meaningful, and those transition times will be determined by the differences in rates before and after the transitions. To control for variables, the two models differed only in their age code but were similar in the area and the ranges of the free parameters (Figure 7B). The initial topographic elevation, which represents the elevation before uplift, is set within a parameter space between 3,450 and 4,570 m, consistent with the highest and lowest elevations of the current Nianchu River, and we use the results to test the rationality of the two models. Details of the thermal and mechanical parameter values used in the inverse models are detailed in Supplementary Table S1.

In an additional simulation of the northern portion, we define a "fault-exhumation scenario" as a scenario that more comprehensively considers the activities of the fault in consideration of our field geological investigations, which showed that the northern and southern portions of the dome were subject to N–S shearing, possibly due to fault activity. The inclination of the set

TABLE 2 Apatite fission track results from the Kangmar dome.

Sample no.	No. of grains	Spontaneous		Induced		Dosimeter		P (χ2) %	Central age (Ma) (±1σ)
		ρs ($\times10^4$ cm^{-2})	Ns	ρi ($\times10^5$ cm^{-2})	Ni	ρd ($\times10^5$ cm^{-2})	Nd		
D0812	40	1.47	43	4.464	1,308	9.107	6,630	88	5.9 ± 0.9
D0813	42	1.46	38	5.316	1,388	10.106	6,630	28.1	5.4 ± 0.9
D0814	42	1.01	55	4.905	2,677	11.102	6,630	11.5	4.3 ± 0.7
D0815	42	0.80	58	4.604	3,318	10.098	6,630	66.5	3.5 ± 0.5
D0816	42	0.59	46	2.111	1,632	8.113	6,630	62.4	4.5 ± 0.7
D0817	42	0.49	35	3.266	2,311	9.109	6,630	12.8	2.7 ± 0.5
D0819	42	1.26	108	6.632	5,671	10.106	6,630	17.5	3.7 ± 0.5
D0820	42	1.16	73	5.485	3,465	11.102	6,630	53.4	4.6 ± 0.6
D7101	42	0.8	31	2.429	947	12.098	6,630	0	8.9 ± 3.9
D7103	42	2.0	97	8.666	4,197	13.094	6,630	34.6	5.9 ± 0.7
D7105	42	1.46	92	6.74	4,236	14.09	6,630	41.2	6.0 ± 0.7
D7107	42	1.62	102	8.046	5,061	15.087	6,630	1.4	5.8 ± 0.8
D7108	42	0.90	79	7.115	6,271	16.083	6,630	0	4.1 ± 0.7
D7109	42	0.58	32	7.065	3,905	17.079	6,630	84.4	2.7 ± 0.5

All samples were dated using the external detector method. The AFT ages were evaluated by the RadialPlotter (Vermeesch, 2009).

fault in that model was consistent with the present day inclination, and the remaining cooling was decoupled to the vertical direction and was expressed by setting a subvertical fault (Figure 7C). In contrast, the initial topographic elevation and transition times of this scenario will adopt the best-fit parameter of the northern "exhumation scenario" to control the number of unknowns (Supplementary Table S2), while other parameters are the same as the first scenario (Supplementary Table S1).

The calculation was supported by the Advanced Computing East China Subcenter. Each inversion procedure contained 19,000 Pecube forward models, and 60 iterations, with 300 sample sizes per iteration and a 33% resampling rate, were applied. The calculation of the misfit function is related to the measured-predicted relationship for each sample.

5.2 Numerical thermo(-kinematic) modeling results

The inversion results from the three models for the two scenarios are listed in Supplementary Table S2. The two models for the exhumation scenario have misfit values of 0.21 and 0.19, and the fault-exhumation scenario has a misfit value of 0.18. As mentioned before, the simulation results from the two models for the initial topo are 4,560 and 4,539 m, respectively, which are similar to the present day topographic elevation differences. Given that their models are based on different parameter settings, this similarity for the common free parameters indicates that the model settings are logical and provides a basis for a joint discussion of the two models (Figure 7B). The lowest-misfit model produces an excellent fit between the predicted and measured ages of the AFT, ZHe and ZFT thermochronometers (Figures 7D–F), and the biotite ^{40}Ar/^{39}Ar ages are distributed in a narrow range of 14–15 Ma, which is consistent with the result reported by Lee et al. (2000). Subsequently, we recalculate the depth-time paths generated from the temperature–time path in the forward model, combined with the average annual temperature of the Earth's surface (8°C) and the geostrophic gradient of 30°C/km.

6 Discussion

We identified inconsistent cooling histories between the northern and southern portions of the Kangmar dome. The modeling directly reveals the cooling histories of the two transects, the velocity of the fault activity and the vertical cooling. However, the interpretation of experimental and modeling results, coupled with geological evidence, is premised on a discussion of the properties of the Nianchu River since the modeled vertical cooling rates do not directly represent the surface uplift rates. Additionally, the flexural response to surface changes should also be considered. However, we believe that the Nianchu River is an antecedent stream river, which is indicated by the K_{sn} analysis results. Under such a premise, the incision of the Nianchu River will always be accompanied by surface uplift, and its rate will increase with increasing surface uplift rate. Then, in the absence of regionally significant climate change, we think that the obtained cooling rates are a positive function of surface uplift or river incision. From this, the results of the modeling scenarios can be used to develop the following discussion.

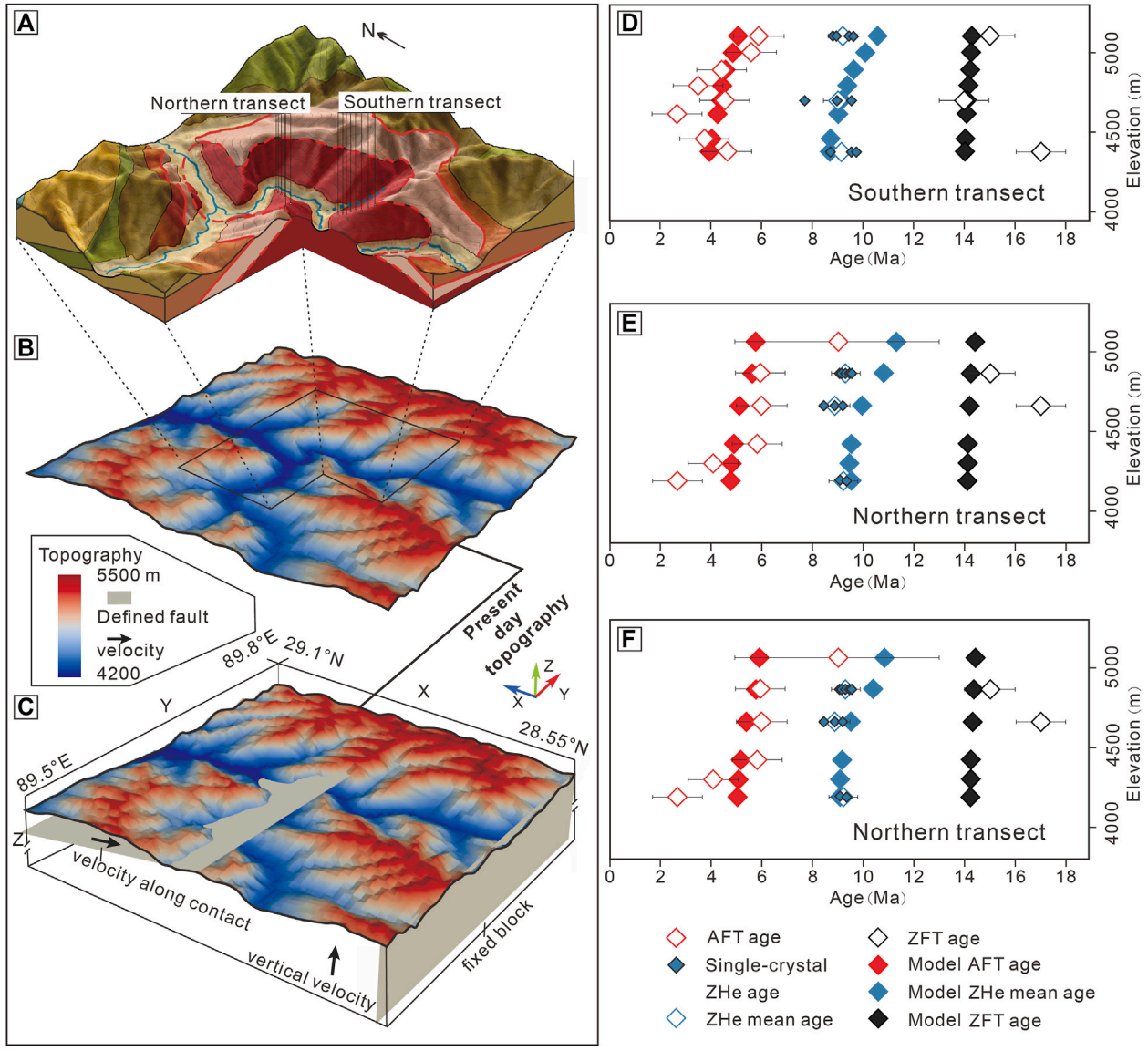

FIGURE 7
(A) Location of the two elevation transects (Refer to Figure 3A legend for details); **(B)** Exhumation scenario and **(C)** Fault-exhumation scenario setup for the 3-D thermokinematic modeling (parameters are given in Supplementary Table S1). Measured and modeled age-elevation relationship of the southern **(D)** and northern **(E)** transects in Exhumation scenario, **(F)** northern transect in Fault-exhumation scenario.

6.1 Geologic affiliation of the core-cover contact fault

Alternatively, the "core–cover contact" fault of the Kangmar dome was defined as follows: 1) the fault is part of a thrust duplex, which was based on observations of tight to isoclinal folds in the top metasedimentary carapace that converged to the south, the reorientation of fold axes to N–S in the lower carapace, and how the shear strain rose with structural depth (Burg et al., 1984); 2) the fault represents the response of a metamorphic core complex-type detachment fault to the gravitational collapse of the Himalayan topographic front (Chen et al., 1990); 3) the fault is a non-conformity with no or minimal displacement (Lee et al., 2000); or 4) the fault indicates a normal-sense (top-to-the-N) brittle–ductile shear zone, equivalent to the STDS (Wagner et al., 2010).

The most remarkable result of our geological analysis is the N–S movement of the fault hanging wall, as reflected by stretching lineation, which distinguishes the Kangmar dome from the diapirism mechanisms of typical domes, such as the Yardoi dome (Zhang et al., 2007) that is located at the easternmost end of the NHGD. The stretching lineation of its core is oriented in a spreading direction to the periphery and extends downward. In the inversion result of the exhumation scenario, the southern portion of the dome experienced its first rapid cooling before 17.7 Ma (Supplementary Table S2; Figure 8A), and the depth contour lines based on depth–time paths reflect that the southern portion was uplifted earlier before the northern portion since ~17.7 Ma and located at a

TABLE 3 Single-grain zircon (U-Th)/He results from the Kangmar dome.

Grain no.	He (ncc)	Mass (mg)	U (ppm)	Th (ppm)	Th/U	Rs (μm)	FT	Corr. Age (Ma)	Error (±1σ)	Weighted mean (Ma ± 1σ)	eU
D0812-1	3.821	0.0058	525.8	269.3	0.51	55.2	0.77	9.1	0.6	9.2 ± 0.5	589.1
D0812-2	13.306	0.0054	1780.8	1,324.4	0.74	57.3	0.77	9.7	0.6		2092.1
D0812-3	3.946	0.0057	548.0	226.6	0.41	54.9	0.77	9.4	0.6		601.2
D0812-4	3.793	0.0051	618.4	308.7	0.50	54.7	0.77	8.8	0.5		691.0
D0816-1	10.684	0.0132	608.8	358.3	0.59	71.0	0.82	9.6	0.6	9.2 ± 0.6	693.0
D0816-2	17.165	0.0113	1,136.7	591.8	0.52	65.8	0.81	9.8	0.6		1,275.8
D0816-3	16.287	0.0104	1,352.7	495.1	0.37	67.8	0.81	8.7	0.5		1,469.0
D0820-1	8.615	0.0061	1,080.8	508.6	0.47	55.1	0.77	9.6	0.6	8.7 ± 0.6	1,200.3
D0820-2	10.892	0.0092	1,169.4	372.1	0.32	64.2	0.80	7.8	0.5		1,256.9
D0820-3	21.529	0.0093	1988.9	459.2	0.23	61.1	0.79	9.1	0.6		2096.8
D7103-1	1.389	0.0059	182.9	98.2	0.54	57.0	0.77	9.3	0.6	9.2 ± 0.5	206.0
D7103-2	13.898	0.0085	1,277.6	530.6	0.42	64.9	0.80	9.5	0.6		1,402.3
D7103-3	8.898	0.0075	965.2	429.2	0.44	61.3	0.79	9.2	0.6		1,066.1
D7103-4	3.055	0.0081	302.2	177.0	0.59	56.7	0.77	9.0	0.6		343.8
D7103-5	12.904	0.0112	912.4	449.9	0.49	67.5	0.81	9.3	0.6		1,018.2
D7105-1	16.019	0.0077	1762.0	803.7	0.46	58.8	0.78	8.8	0.5	8.9 ± 0.6	1950.9
D7105-2	22.598	0.0118	1,583.1	441.0	0.28	77.6	0.83	9.3	0.6		1,686.7
D7105-3	29.928	0.0129	2045.5	791.0	0.39	73.6	0.83	8.5	0.5		2,231.4
D7109-1	14.789	0.0104	1,197.4	233.7	0.20	65.8	0.81	9.3	0.6	9.2 ± 0.5	1,252.3
D7109-2	19.878	0.0090	1702.1	1,057.6	0.62	65.7	0.80	9.3	0.6		1950.6
D7109-3	8.246	0.0075	868.0	430.8	0.50	58.0	0.78	9.3	0.6		969.3
D7109-4	12.026	0.0137	772.9	157.0	0.20	73.7	0.83	8.9	0.6		809.8

Rs is the sphere equivalent radius of hexagonal crystal (Beucher et al., 2013); F_T is the alpha-ejection correction after Farley et al. (1996); Weighted means at 95% confidence level calculated using Isoplot V3.59 (Ludwig, 1992).

10.3389/feart.2023.1186901

TABLE 4 Zircon fission track results from the Kangmar dome.

Sample no.	No. of grains	Spontaneous		Induced		Dosimeter		P (χ2) %	Central age (Ma) (±1σ)
		ρs ($\times10^5$ cm^{-2})	Ns	ρi ($\times10^5$ cm^{-2})	Ni	ρd ($\times10^5$ cm^{-2})	Nd		
D0812	36	40.508	3,524	122.776	10,681	10.346	6,844	0	15.0 ± 0.7
D0816	36	28.893	2,292	91.657	7,271	9.775	6,844	0.5	13.6 ± 0.6
D0820	36	47.133	3,739	154.699	12,272	13.128	6,844	0	17.3 ± 0.9
D7103	37	39.792	3,540	149.447	13,295	12.486	6,844	0.2	14.7 ± 0.6
D7105	36	42.508	3,393	132.975	10,614	11.844	6,844	0	16.8 ± 0.8

All samples were dated using the external detector method. The ZFT ages were evaluated by the RadialPlotter (Vermeesch, 2009).

shallower depth until ~5 Ma (Figure 9). Since the activity of the fault somehow affects the kinematic features of the gneiss core, the significant variation in uplift histories of the two portions in such a limited area is, we believe, related to the differential properties of the core-cover contact fault at each side. Furthermore, the intersection depth of the biotite ^{40}Ar/^{39}Ar isotherm in the northern portion is deeper than it is in reality. In comparison, the biotite intersection depth in the south portion is shallower (Figure 9), suggesting that the isotherm within the south portion has shifted upward at this stage. These differences could be explained by the thrust-sense faulting of the hanging wall in the south portion, which is consistent with the geological evidence that the southern strata are thicker (Figure 6) and the present day structures indicating top-to-the-N shearing (Figure 5). Thus, the northward movement of the cover strata caused the first rapid cooling in the southern portion, and this rapid cooling event started earlier than the starting time of our simulation models at 20 Ma.

In the exhumation scenario, the first rapid cooling of the northern portion began at ~12.2 Ma, and after the inversion of the fault-exhumation scenario, we detailed the effects of vertical cooling or cooling along the fault and the results show that rapid cooling began at ~12.2 Ma and was oriented mainly along the fault (Figure 8B). Although this timing is consistent with the ^{40}Ar/^{39}Ar age of ~13.23 Ma, which was derived from the analysis of syn-deformation muscovite from the mylonitic garnet two-mica schist within the fault shear zone and was interpreted as the initial detaching time of the core-cover contact fault (Wang et al., 2015), we do not consider that this phase of rapid cooling was controlled by fault activity, but instead, we believe that the doming event of the north portion was the direct cause of cooling. The doming of the gneiss core increases the dip of the fault, which leads to the emergence of cooling velocities along the fault. According to the forward-modeled depth isochrons (Figure 9), the northern transect started to dramatically uplift after 12 Ma, and the doming event first occurred in the northern portion at 12.2 Ma, much later than it did in the south. Since the core-cover contact fault of the Kangmar dome was a continuous interface exposed from north to south without interruption, it is reasonable to infer that the cover strata of the northern portion also had a consistent northward movement history before its doming event.

Our simulations showed that the cover strata above the Kangmar gneiss core had the same northward movement as the STDS in the Miocene and were consistent with the geological evidence characterized by the extensive distribution of stress formations in both the gneiss core and cover (Figure 3A), which revealed a N–S movement of the cover strata. As discussed below, considering that the onset time of the dome and its location is coincident with the STDS, we concur with the suggestion of Chen et al. (1990), Hauck et al. (1998), and Liu et al. (2016) that this fault is the northern continuation of the STDS and is an exposed portion of the Tethyan Himalayan sedimentary sequence.

6.2 Rapid cooling history of the dome

6.2.1 Post-middle Miocene rapid cooling

In our simulations, the timing of the doming event in the southern portion precedes that in the northern portion, and the core of the Kangmar dome has been experiencing rapid cooling since the Miocene and the northern portion had a higher cooling rate from 12.2 to 9.1 Ma and a more consistent cooling rate after 9.1 Ma and before 1.8 Ma. We believe that the core-cover contact fault of the Kangmar dome is subordinate to the STDS. The rapid cooling of the northern portion of the Kangmar dome at ~12 Ma, which accompanied doming during this period, was caused by the northward sliding of the STDS. However, present day studies suggest that the more short-lived southern STDS ended prior to 11 Ma (Dong, et al., 2021; Figure 8D). The northward movement of the upper strata could not cause the rapid cooling of the southern portion. Since there are many E–W extensional structures above the dome (e.g., Figures 4C, D), we take the N–S trending rift's impact on dome cooling. Wang et al. (2022) concluded from fault gouge studies that the Pari-Duoqingcuo graben (Figure 2A) was active earlier than 9 Ma and that the activity of the Yadong-Gulu Rift was consistent and continuous. Bian et al. (2022) further inverted the thermochronological data of the Yadong area and concluded that the onset of rifting occurred at 12 Ma (Figure 8D), which coincides with our modeled results for the rapid cooling of the northern portion. It is plausible that the E–W extension of the Yadong-Gulu Rift may have triggered the uplift of the dome core by vertically thinning the cover strata, thereby causing this phase of rapid cooling. However, this explanation still needs more geological evidence and discussion.

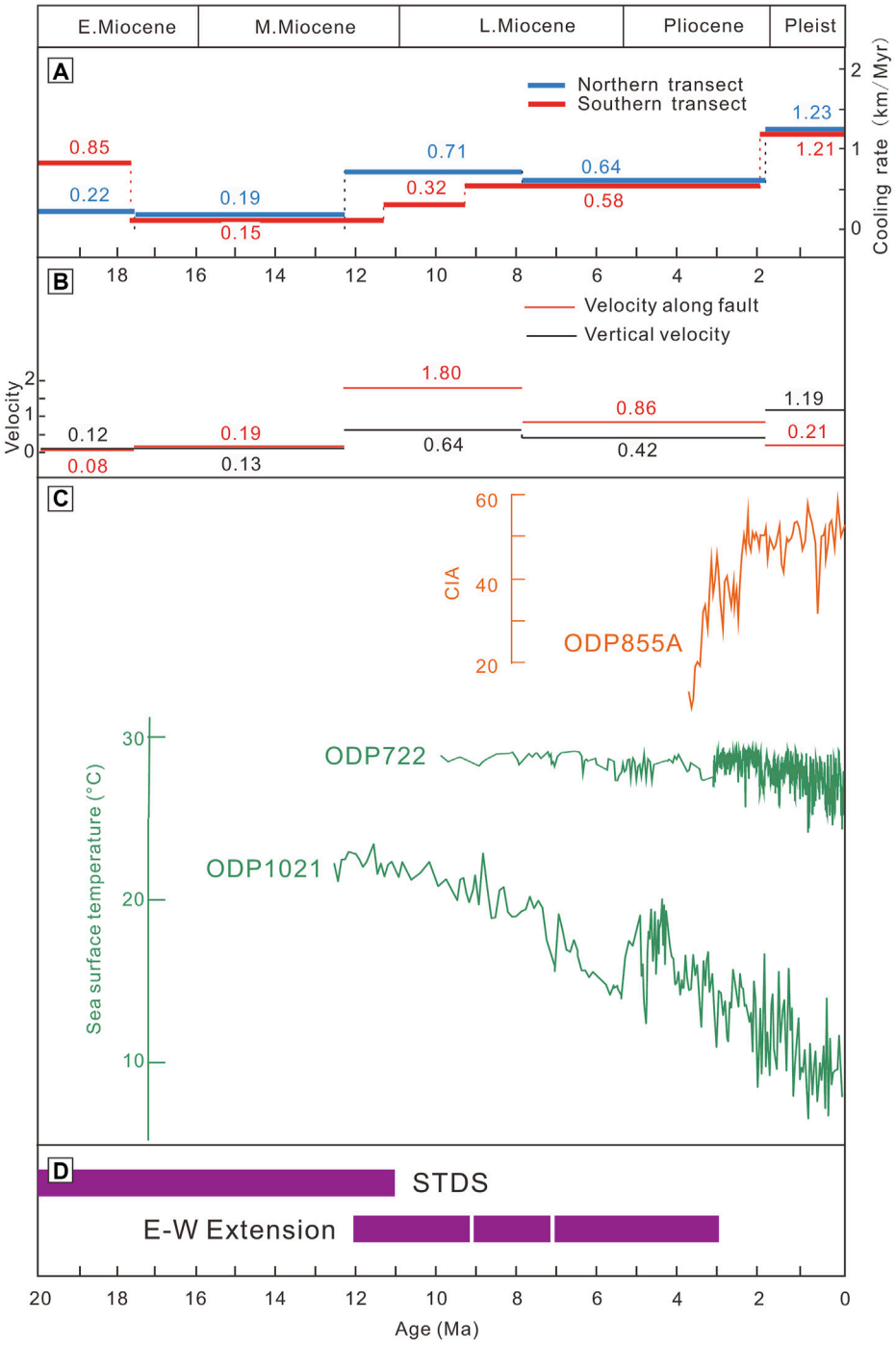

FIGURE 8
Graphical representation of the best-fit inversion result of the cooling rate from the exhumation scenario **(A)** and/or velocity from fault-exhumation scenario **(B)**; **(C)** the chemical index of alteration (CIA) data from Ocean Drilling Program (ODP) Hole 885A, North Pacific Ocean (Zhang., et, al. 2019), the sea surface temperature data from Ocean Drilling Program (ODP) Hole 722 in Arabian Sea and 1021 in North Pacific Ocean (Herbert and Lawrence, 2016); **(D)** Tectonic activities in the Kangmar-Yadong area, southern Tibet. Timing of the STDS (Webb et al., 2017; Dong et al., 2021) and E–W extension (Dong et al., 2021; Bian et al., 2022; Wang et al., 2022).

6.2.2 Pleistocene rapid cooling

If the northward sliding of the STDS and the tectonic action of vertical thinning of the THS due to the E–W extension of the Yadong-Gulu rift are plausible explanations for the Miocene rapid cooling of the Kangmar dome, the activity in the Yadong-Gulu Rift, which was not significantly accelerated in the Pleistocene, would not have caused the rapid cooling event starting after ~1.8 Ma. The extensive present day pale glacial remains and very low modern glacial cover of the Kangmar dome prevent us from ignoring glacial activity over the geological-

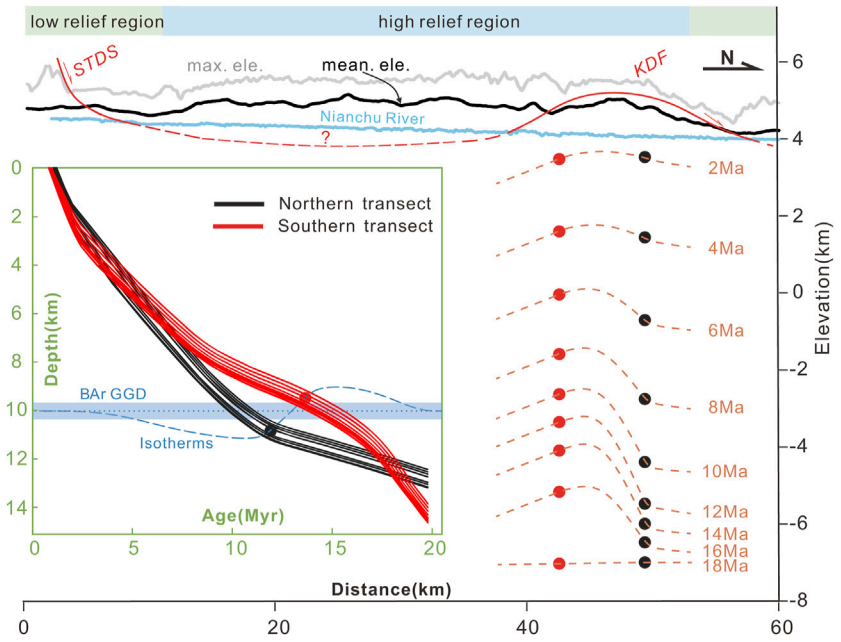

FIGURE 9
Topographic profiles, averaged equilibrium line altitudes (ELAs), and exhumation patterns (depth isochrones) along a south–north swath across the Kangmar dome. The swath is part of Figure 2B. The curves in the green box represent the depth–time path of the two transects generated from their best-fit model, note that the blue dotted line represents the isotherms (assuming that the south portion takes the B-Ar value of ~14 Ma, the north ~12 Ma), GGD, Geothermal-Gradient Depth. The orange lines represent the depth isochrones generated from the depth–time path.

historical period within its region. At this stage, climatic events on the Tibetan Plateau coincided with global climatic events (Ji et al., 2013), and sea surface temperature changes reflected in boreholes from the North Pacific (ODP1021) and Indian Ocean (ODP722) (Herbert and Laerence, 2016) show that the Earth's climate changed markedly during the Pliocene (Figure 8C), with a general trend of variable cooling over time. According to our simulations, the Pleistocene rapid cooling of the gneiss core is temporally similar to this rapid global cooling of sea surface temperature. Zhang et al. (2019) revealed the enhanced chemical alteration in the Asian hinterlands through the changes in the chemical index of alteration (CIA) of the core sediments from ODP885A in the North Pacific Ocean and attributed it to the increased surface exhumation caused by increased inland glaciation (Figure 8C). We suggest that the enhanced glacial activity of the Kangmar dome region in the context of this phase of rapid global cooling during the Pleistocene may have directly intensified surface exhumation, and at the same time, the increase in glacial melt water further strengthened the incision of the Nianchu River. This joint action may have caused rapid cooling since ~1.8.

6.3 Evolution of the dome and its implications

After the doming event occurred in the Miocene, our modeling results revealed a northward movement along the STDS, which differed significantly from the "gravitational collapse" model in terms of fault movement properties. However, Chen et al. (1990) argued that the dome developed via mechanisms similar to the metamorphic core complexes (MCC) in Cordilleran regions. Our fault-modeling results agree with this fault affiliation. With an absence of essential components, e.g., detachment systems, hanging-wall extension faults, and basins, the mechanism based on simple linkage with typical MCC is seemingly unreasonable.

In light of an "inverted" pattern in which the mica cooling ages increased toward deeper structural levels and decreased northward at the same level, Lee et al. (2000) proposed that the doming event resulted from the thrusting of the hanging wall mid-crustal rocks along the north-dipping Gyirong-Kangmar thrust fault (GKT) (Figure 3C). Wang et al. (2022) modified the movement nature of the core-cover contact and tested a mid-crustal "channel-flow" model that solved its dynamic origin. However, the mechanism of "thrust along the GKT" does not fit our measured age based on a lower closure temperature that shows an increasing trend from south to north (Figures 7D, E), nor could it adequately explain the various slipping histories of the core-cover contact fault between the southern and northern portions. The core-cover contact fault around the Kangmar dome has been imaged as continuous and high-amplitude reflection events at relatively shallow depths along the INDEPTH seismic reflection profile (Nelson et al., 1996; Zhao et al., 1993). Liu et al. (2006) confirmed that the dip angle of the mid-crustal reflection formed by the Main Himalayan Thrust (MHT) increases progressively with its northward extension and that the MHT continues north of the Kangmar dome. The thrust stacking above the MHT detected by the most recent

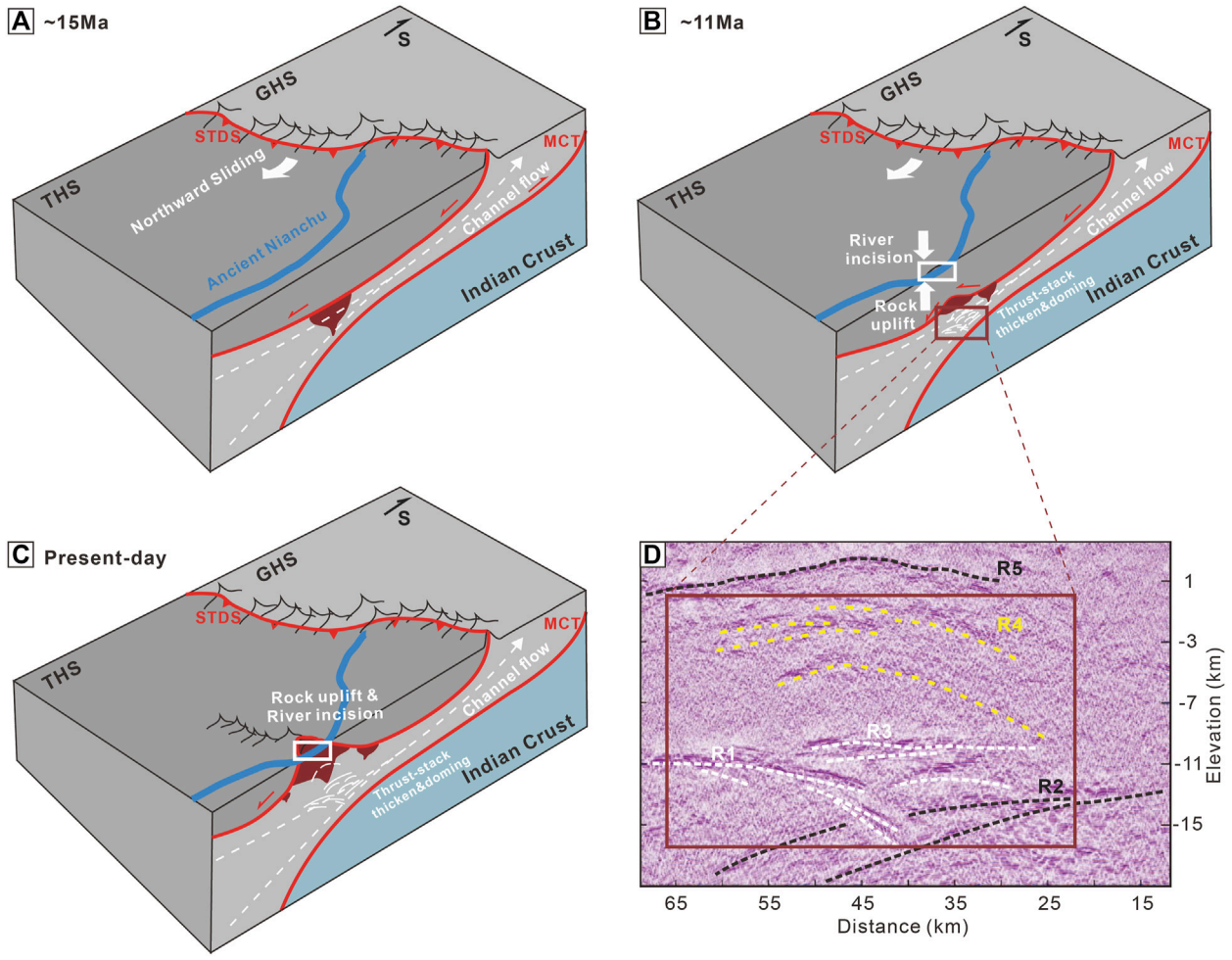

FIGURE 10
Proposed model for the evolution of the Kangmar dome. **(A)** Top-down-to-N sliding related to the detachment of the STDS and the southward extrusion of the GHC; **(B)** doming expressed from local crustal thickening caused by stacked thrusts and the associated incision of the Nianchu River. Note that the detachment of the STDS persisted, and the YGR became active at some approximate later time. **(C)** Continued fast cooling due to glacier activity; **(D)** interpretation of the deep seismic reflection profile image by Li et al. (2021). R1-R5 are relatively high reflections. R1, R2, and R3 are parts of a thrust decollement, possibly the MCT. R4 represents the consequent doming, and R5 is interpreted to be the STDS shear zone. MCT, Main Central thrust; STDS, Southern Tibetan detachment system; THS, Tethys Himalaya Sequence; GHS, Grater Himalaya sequence; YGR, Yadong-Gulu rift.

regional N–S trending seismic profile (Li et al., 2021) between the Mabja dome and Kampa dome was interpreted as the cause of the doming event. However, the GKT was not observed at the corresponding depth in either seismic profile, and the STDS was identified at a depth of 3–3.5 km as a continuous interface overlying the high-velocity body and extending northward for a considerable distance (Figure 10D). Although the profile is located in a rift between the Mabja dome and the Kampa dome, where the STDS is not yet exposed, it is reasonable to assume that the crustal morphology it reflects is intermediate in the evolution of other domes. The "thrust stacks" at depths of 11–20 km, which are considered to control the formation of the Mabja dome, could also be transplanted to explain the cause of the Kangmar doming event (Figure 10B), and with the latest sensible application of channel flow reported by Chen et al. (2022), we further infer that the "thrust stack" in the lower-middle crust is related to the southward flowing channel flow.

Overall, the northward sliding of the THS related to the detachment of the STDS since ~20 Ma resulted in the N-S-trending stretching lineation of the gneiss core and dominated the earlier uplift of the southern portion (Figure 10A). Note that the incision of the Nianchu River was always accompanied by the surface uplift of the dome. The doming event that occurred at ~12.2 Ma was caused by the thrust stack, which was related to the southward flowing channel flow. Since the activities of the STDS located south of the Kangmar dome ceased before 11 Ma, the following uplifting of the dome might be associated with the N–S trending Yadong-Gulu rift and its associated persistent thinning in the upper crust (Figure 10B), which caused the existence of E–W extensional structures. The Pleistocene rapid cooling was attributed to enhanced glacial activity, and the incision of the Nianchu River formed the present Kangmar dome landscape (Figure 10C).

7 Conclusion

We present new (U-Th)/He and fission track data from two elevation transects across the Kangmar dome. Based on geological mapping and our new numerical modeling results, we demonstrate distinct cooling histories within the different portions of the Kangmar dome. We suggest that the core-cover contact fault was the northern continuation of the STDS exposed in the THS. We argue that the two phases of rapid cooling events during the Miocene and the Pleistocene resulted from regional extension structures and enhanced glacial activity, respectively. Combined with previous studies, we proposed a new model in which the development of the Kangmar dome was dominated by a thrust stack associated with the southward flowing channel flow, which challenges the previous models of southward thrusting along the GKT.

Data availability statement

The original contributions presented in the study are included in the article/Supplementary Material, further inquiries can be directed to the corresponding author.

Author contributions

ZM, ZH, and YL designed this study. ZM, ZH, and TX discussed. ZM, TX, and WZ contributed to the modeling. XH performed the channel steepness index analysis. ZM and ZH interpreted the data and wrote the manuscript. ZH, WB, and WZ contributed to sampling and testing. All authors contributed to the revision of the text.

Funding

This work was supported by the National Natural Science Foundation of China (Grant No. 42121002), the Second Tibetan Plateau Scientific Expedition and Research Program (STEP) (Grant No. 2019QZKK0204), the China Geological Survey (Grant No. DD20190057), and the Fundamental Research Funds for the Central Universities (Grant No. 35732020069).

Conflict of interest

The authors declare that the research was conducted in the absence of any commercial or financial relationships that could be construed as a potential conflict of interest.

Publisher's note

All claims expressed in this article are solely those of the authors and do not necessarily represent those of their affiliated organizations, or those of the publisher, the editors and the reviewers. Any product that may be evaluated in this article, or claim that may be made by its manufacturer, is not guaranteed or endorsed by the publisher.

Supplementary material

The Supplementary Material for this article can be found online at: https://www.frontiersin.org/articles/10.3389/feart.2023.1186901/full#supplementary-material

References

Aikman, A. B., Harrison, T. M., and Lin, D. (2008). Evidence for early (>44 ma) himalayan crustal thickening, tethyan Himalaya, southeastern tibet. *Earth Planet. Sci. Lett.* 274 (1-2), 14–23. doi:10.1016/j.epsl.2008.06.038

Aoya, M., Wallis, S. R., Kawakami, T., Lee, J., Wang, Y., and Maeda, H. (2006). The Malashan gneiss dome in south Tibet: Comparative study with the Kangmar dome with special reference to kinematics of deformation and origin of associated granites. *Geol. Soc. Lond. Spec. Publ.* 268 (1), 471–495. doi:10.1144/GSL.SP.2006.268.01.22

Aoya, M., Wallis, S. R., Terada, K., Lee, J., Kawakami, T., Wang, Y., et al. (2005). North-south extension in the Tibetan crust triggered by granite emplacement. *Geology* 33 (11), 853–856. doi:10.1130/G21806.1

Ault, A. K., Gautheron, C., and King, G. E. (2019). Innovations in (U–Th)/He, fission track, and trapped charge thermochronometry with applications to earthquakes, weathering, surface–mantle connections, and the growth and decay of mountains. *Tectonics* 38, 3705–3739. doi:10.1029/2018TC005312

Beaumont, C., Jamieson, R. A., Nguyen, M. H., and Lee, B. (2001). Himalayan tectonics explained by extrusion of a low-viscosity crustal channel coupled to focused surface denudation. *Nature* 414 (6865), 738–742. doi:10.1038/414738a

Beaumont, C., Jamieson, R. A., Nguyen, M. H., and Medvedev, S. (2004). Crustal channel flows: 1. Numerical models with applications to the tectonics of the himalayan-Tibetan orogen. *J. Geophys. Res. Solid Earth* 109 (6), 1. doi:10.1029/2003JB002809

Beucher, R., Brown, R. W., Roper, S., Stuart, F., and Persano, C. (2013). Natural age dispersion arising from the analysis of broken crystals: Part II. Practical application to apatite (U–Th)/He thermochronometry. *Geochimica Cosmochimica Acta* 120, 395–416. doi:10.1016/j.gca.2013.05.042

Bi, W., Li, Y., Kamp, P. J., Xu, G., Zhang, J., Han, Z., et al. (2022). Cretaceous–Cenozoic cooling history of the Qiangtang terrane and implications for Central Tibet formation. *GSA Bull.*, doi:10.1130/B36313.1

Bian, S., Gong, J., Zuza, A. V., Yang, R., Chen, L., Ji, J., et al. (2022). Along-strike variation in the initiation timing of the north-trending rifts in southern Tibet as revealed from the Yadong-Gulu rift. *Tectonics* 41 (7), e2021TC007091. doi:10.1029/2021TC007091

Braun, J. (2003). Pecube: A new finite-element code to solve the 3D heat transport equation including the effects of a time-varying, finite amplitude surface topography. *Comput. Geosciences* 29 (6), 787–794. doi:10.1016/S0098-3004(03)00052-9

Braun, J., van der Beek, P., Valla, P., Robert, X., Herman, F., Glotzbach, C., et al. (2012). Quantifying rates of landscape evolution and tectonic processes by thermochronology and numerical modeling of crustal heat transport using PECUBE. *Tectonophysics* 524-525, 1–28. doi:10.1016/j.tecto.2011.12.035

Burg, J. P., Guiraud, M., Chen, G. M., and Li, G. C. (1984). Himalayan metamorphism and deformations in the North Himalayan Belt (southern Tibet, China). *Earth and Planet. Sci. Lett.* 69 (2), 391–400. doi:10.1016/0012-821X(84)90197-3

Chen, S., Zhang, B., Zhang, J., Wang, Y., Li, X., ZhangL& Yue, Y., et al. (2022). Tectonic transformation from orogen-perpendicular to orogen-parallel extension in the North Himalayan Gneiss Domes: Evidence from a structural, kinematic, and geochronological investigation of the Ramba gneiss dome. *J. Struct. Geol.* 155, 104527. doi:10.1016/j.jsg.2022.104527

Chen, X. (1979). K-Ar Dating and division of the Himalayan movement in southern Xizang. *Chin. J. Geol.* 14 (1), 13–21. (in Chinese with English abstract).

Chen, Z., Liu, Y., Hodges, K. V., Burchfiel, B. C., Royden, L. H., and Deng, C. (1990). The kangmar dome: A metamorphic core complex in southern xizang (tibet). *Science* 250 (4987), 1552–1556. doi:10.1126/science.250.4987.1552

Coney, P. J., Crittenden, M. D., and Davis, G. H. (1980). Cordilleran metamorphic core complexes: An overview. *Cordilleran Metamorph. core complexes* 153, 7–31. doi:10.1130/MEM153-p7

Debon, F. (1980). Genesis of the three concentrically-zoned granitoid plutons of Cauterets-Panticosa (French and Spanish western Pyrenees). *Geol. Rundsch.* 69 (1), 107–130.

Ding, H., Zhang, Z., Dong, X., Tian, Z., Xiang, H., Mu, H., et al. (2016). Early Eocene (c. 50 ma) collision of the Indian and asian continents: Constraints from the North himalayan metamorphic rocks, southeastern tibet. *Earth Planet. Sci. Lett.* 435, 64–73. doi:10.1016/j.epsl.2015.12.006

Dong, H., Larson, K. P., Kellett, D. A., Xu, Z., Li, G., Cao, H., et al. (2021). Timing of slip across the South Tibetan detachment system and yadong–gulu graben, eastern Himalaya. *J. Geol. Soc.* 178 (1), 1. doi:10.1144/jgs2019-197

Eskola, P. E. (1949). The problem of mantled gneiss domes. *Geol. Soc. Lond. Q. J.* 104, 461. doi:10.1144/GSL.JGS.1948.104.01-04.2

Galbraith, R. F., and Laslett, G. M. (1993). Statistical models for mixed fission track ages. *Nuclear tracks and radiation measurements* 21 (4), 459–470. doi:10.1016/1359-0189(93)90185-C

Gao, L. E., and Zeng, L. (2014). Fluxed melting of metapelite and the formation of Miocene high-CaO two-mica granites in the Malashan gneiss dome, southern Tibet. *Geochimica Cosmochimica Acta* 130, 136–155. doi:10.1016/j.gca.2014.01.003

Gao, L. E., Zeng, L., Hu, G., Wang, Y., Wang, Q., Guo, C., et al. (2019). Early paleozoic magmatism along the northern margin of east gondwana. *Lithos* 334, 25–41. doi:10.1016/j.lithos.2019.03.007

Gao, L., Zeng, L., and Xie, K. (2012). Eocene high grade metamorphism and crustal anatexis in the North Himalaya gneiss domes, southern tibet. *Chin. Sci. Bull.* 57 (6), 639–650. doi:10.1007/s11434-011-4805-4

Gleadow, A. J., Duddy, I. R., Green, P. F., and Lovering, J. F. (1986). Confined fission track lengths in apatite: A diagnostic tool for thermal history analysis. *Contributions Mineralogy Petrology* 94, 245–254. doi:10.1016/0012-821X(86)90065-8

Guenthner, W. R., Reiners, P. W., Ketcham, R. A., Nasdala, L., and Giester, G. (2013). Helium diffusion in natural zircon: Radiation damage, anisotropy, and the interpretation of zircon (U-Th)/He thermochronology. *Am. J. Sci.* 313 (3), 145–198. doi:10.2475/03.2013.01

Guo, L., Zhang, J., and Zhang, B. (2008). Structures, kinematics, thermochronology and tectonic evolution of the Ramba gneiss dome in the northern Himalaya. *Prog. Nat. Sci.* 18 (7), 851–860. doi:10.1016/j.pnsc.2008.01.016

Harrison, T. M., Ryerson, F. J., Le Fort, P., Yin, A., Lovera, O. M., and Catlos, E. J. (1997). A late Miocene-Pliocene origin for the central Himalayan inverted metamorphism. *Earth Planet. Sci. Lett.* 146 (1-2), E1–E7. doi:10.1016/S0012-821X(96)00215-4

Hauck, M. L., Nelson, K. D., Brown, L. D., Zhao, W., and Ross, A. R. (1998). Crustal structure of the Himalayan orogen at~ 90 east longitude from Project INDEPTH deep reflection profiles. *Tectonics* 17 (4), 481–500. doi:10.1029/98TC01314

Herbert, T., Lawrence, K., Peterson, L. C., Caballero-Gill, R., Kelly, C. S., et al. (2016). Late Miocene global cooling and the rise of modern ecosystems. *Nat. Geosci.* 9, 843–847. doi:10.1038/ngeo2813

Jessup, M. J., Langille, J. M., Diedesch, T. F., and Cottle, J. M. (2019). Gneiss dome formation in the Himalaya and southern Tibet. *Geol. Soc. Lond. Spec. Publ.* 483 (1), 401–422. doi:10.1144/SP483.15

Ji, J. L., Hong, H. L., Xiao, G. Q., Lin, X., and Xu, Y. D. (2013). Evolutionary sequences of the Neogene major climatic events in the Tibetan Plateau. *Geol. Bull. China* 32 (1), 120–129. (in Chinese with English abstract).

Ji, W. Q., Wu, F. Y., Wang, J. M., Liu, X. C., Liu, Z. C., Zhang, Z., et al. (2020). Early evolution of himalayan orogenic belt and generation of middle Eocene magmatism: Constraint from haweng granodiorite porphyry in the tethyan Himalaya. *Front. Earth Sci.* 8, 236. doi:10.3389/feart.2020.00236

Kawakami, T., Aoya, M., Wallis, S. R., Lee, J., Terada, K., Wang, Y., et al. (2007). Contact metamorphism in the malashan dome, North Himalayan gneiss domes, southern tibet: An example of shallow extensional tectonics in the Tethys Himalaya. *J. Metamorph. Geol.* 25 (8), 831–853. doi:10.1111/j.1525-1314.2007.00731.x

Ketcham, R. A., Carter, A., Donelick, R. A., Barbarand, J., and Hurford, A. J. (2007). Improved modeling of fission-track annealing in apatite. *Am. Mineralogist* 92 (5–6), 799–810. doi:10.2138/am.2007.2281

King, J., Harris, N., Argles, T., Parrish, R., and Zhang, H. (2011). Contribution of crustal anatexis to the tectonic evolution of Indian crust beneath southern Tibet. *Bulletin* 123 (1-2), 218–239. doi:10.1130/B30085.1

Kirby, E., Whipple, K. X., Tang, W., and Chen, Z. (2003). Distribution of active rock uplift along the eastern margin of the Tibetan Plateau: Inferences from bedrock channel longitudinal profiles. *J. Geophys. Res. Solid Earth* 108 (4), 1. doi:10.1029/2001JB000861

Larson, K. P., Godin, L., Davis, W. J., and Davis, D. W. (2010). Out-of-sequence deformation and expansion of the Himalayan orogenic wedge: Insight from the Changgo culmination, south central Tibet. *Tectonics* 29 (4), 1. doi:10.1029/2008TC002393

Le Fort, P., Cuney, M., Deniel, C., France-Lanord, C., Sheppard, S. M. F., Upreti, B. N., et al. (1987). Crustal generation of the Himalayan leucogranites. *Tectonophysics* 134 (1-3), 39–57. doi:10.1016/0040-1951(87)90248-4

Lee, J., Hacker, B. R., Dinklage, W. S., Wang, Y., Gans, P., Calvert, A., et al. (2000). Evolution of the kangmar dome, southern tibet: Structural, petrologic, and thermochronologic constraints. *Tectonics* 19 (5), 872–895. doi:10.1029/1999TC001147

Lee, J., Hacker, B., and Wang, Y. (2004). Evolution of North Himalayan gneiss domes: Structural and metamorphic studies in Mabja dome, southern tibet. *J. Struct. Geol.* 26 (12), 2297–2316. doi:10.1016/j.jsg.2004.02.013

Lee, J., McClelland, W., Wang, Y., Blythe, A., and McWilliams, M. (2006). Oligocene-miocene middle crustal flow in southern tibet: Geochronology of Mabja dome. *Geol. Soc. Lond. Spec. Publ.* 268 (1), 445–469. doi:10.1144/gsl.sp.2006.268.01.21

Li, H. Q., Gao, R., Li, W. H., Carbonell, R., Yelisetti, S., Huang, X. F., et al. (2021). The Mabja dome structure in southern Tibet revealed by deepseismic reflection data and its tectonic implications. *J. Geophys Res-Solid Earth* 126, e20265. doi:10.1029/2020JB020265

Li, Y., Wang, C., Dai, J., Xu, G., Hou, Y., and Li, X. (2015). Propagation of the deformation and growth of the Tibetan–himalayan orogen: A review. *Earth-Science Rev.* 143, 36–61. doi:10.1016/j.earscirev.2015.01.001

Li, Y., Wang, C., Zhao, X., Yin, A., and Ma, C. (2012). Cenozoic thrust system, basin evolution, and uplift of the Tanggula Range in the Tuotuohe region, central Tibet. *Gondwana Res.* 22 (2), 482–492. doi:10.1016/j.gr.2011.11.017

Liang, W., Resentini, A., Guo, R., and Garzanti, E. (2020). Multimineral fingerprinting of modern sand generated from the Tethys Himalaya (Nianchu River, tibet). *Sediment. Geol.* 399, 105604. doi:10.1016/j.sedgeo.2020.105604

Liu, K., Zhao, W. J., Jiang, W., and Wu, Z. H. (2006). Where is the northern margin of the Indian plate? *Geol. Bull. China* 25 (1-2), 43–47. (in Chinese with English abstract).

Liu, W. C., Wang, Y., Zhang, X. X., Min, L. H., Zhou, Z. G., and Zhao, X. G. (2004). The rock types and isotope dating of the kangmar gneissic dome in southern tibet. *Earth Sci. Front.* 11 (4), 491–501. (in Chinese with English abstract).

Liu, X. C., Wu, F. Y., Yu, L. J., Liu, Z. C., Ji, W. Q., and Wang, J. G. (2016). Emplacement age of leucogranite in the Kampa dome, southern tibet. *Tectonophysics* 667, 163–175. doi:10.1016/j.tecto.2015.12.001

Liu, Z. C., Wu, F. Y., Ji, W. Q., Wang, J. G., and Liu, C. Z. (2014). Petrogenesis of the Ramba leucogranite in the Tethyan Himalaya and constraints on the channel flow model. *Lithos* 208, 118–136. doi:10.1016/j.lithos.2014.08.022

Ludwig, R. K. (1992). *ISOPLOT a plotting and regression program for radiogenic-isotope data, version 2.57*. USA: US Geol. Surv., Open File Rept., 40.

Mancktelow, N. S., and Pavlis, T. L. (1994). Fold-fault relationships in low-angle detachment systems. *Tectonics* 13 (3), 668–685. doi:10.1029/93TC03489

Mattauer, M., Brunel, M., and Matte, P. (1988). Failles normales ductiles et grands chevauchements. Une nouvelle analogie entre l'Himalaya et la chaîne hercynienne du Massif Central français. *Comptes rendus l'Académie Sci. Série 2, Mécanique, Phys. Chim. Sci. l'univers, Sci. Terre* 306 (10), 671–676.

Meng, J., Wang, C., Zhao, X., Coe, R., Li, Y., and Finn, D. (2012). India-asia collision was at 24 N and 50 ma: Palaeomagnetic proof from southernmost asia. *Sci. Rep.* 2 (1), 925–1011. doi:10.1038/srep00925

Miller, E. L., Calvert, A. T., and Little, T. A. (1992). Strain-collapsed metamorphic isograds in a sillimanite gneiss dome, Seward Peninsula, Alaska. *Geology* 20 (6), 487–490. doi:10.1130/0091-7613(1992)020<0487:SCMIIA>2.3.CO;2

Molnar, P., and Tapponnier, P. (1975). Cenozoic Tectonics of Asia: Effects of a Continental Collision: Features of recent continental tectonics in Asia can be interpreted as results of the India-Eurasia collision. *Science* 189 (4201), 419–426. doi:10.1126/science.189.4201.419

Nelson, K. D., Zhao, W., Brown, L. D., Kuo, J., Che, J., Liu, X., et al. (1996). Partially molten middle crust beneath southern Tibet: Synthesis of project INDEPTH results. *science* 274 (5293), 1684–1688. doi:10.1126/science.274.5293.1684

Ou, X., Replumaz, A., and van der Beek, P. (2021). Contrasting exhumation histories and relief development within the Three Rivers Region (south-east Tibet). *Solid earth.* 12 (3), 563–580. doi:10.5194/se-12-563-2021

Quigley, M. C., Liangjun, Y., Gregory, C., Corvino, A., Sandiford, M., Wilson, C. J. L., et al. (2008). U–Pb SHRIMP zircon geochronology and T–t–d history of the Kampa Dome, southern Tibet. *Tectonophysics* 446 (1-4), 97–113. doi:10.1016/j.tecto.2007.11.004

Quigley, M., Liangjun, Y., Xiaohan, L., Wilson, C. J., Sandiford, M., and Phillips, D. (2006). 40Ar/39Ar thermochronology of the Kampa Dome, southern Tibet: Implications for tectonic evolution of the North Himalayan gneiss domes. *Tectonophysics* 421 (3-4), 269–297. doi:10.1016/j.tecto.2006.05.002

Ramberg, H. (1980). Diapirism and gravity collapse in the scandinavian caledonides. *J. Geol. Soc.* 137 (3), 261–270. doi:10.1144/gsjgs.137.3.0261

Ramsay, J. G., (1967), *Folding and fracturing of rocks*. Mc Graw Hill Book Company, 568.

Ratschbacher, L., Frisch, W., Liu, G., and Chen, L., (1994), Distributed deformation in southern and western Tibet during and after the India-Asia collision, *J. Geophys. Res. Solid Earth*, 99 (B10), 19917–19945. doi:10.1029/94JB00932

Reiners, P. W., (2005), Zircon (U-Th)/He thermochronometry, *Rev. Mineral. Geochem.*, 58, 151–179. doi:10.2138/rmg.2005.58.6

Reiners, P. W., and Shuster, D. L. (2009). Thermochronology and landscape evolution. *Phys. Today* 62, 31–36. doi:10.1063/1.3226750

Sambridge, M. (1999b). Geophysical inversion with a neighbourhood algorithm-II. Appraising the ensemble. *Geophys. J. Int.* 138 (3), 727–746. doi:10.1046/j.1365-246x.1999.00900.x

Sambridge, M. (1999a). Geophysical inversion with a neighbourhood algorithm-I. Searching a parameter space. *Geophys. J. Int.* 138 (2), 479–494. doi:10.1046/j.1365-246X.1999.00876.x

Schärer, U., Xu, R. H., and Allègre, C. J. (1986). U (Th) Pb systematics and ages of Himalayan leucogranites, South Tibet. *Earth Planet. Sci. Lett.* 77 (1), 35–48. doi:10.1016/0012-821X(86)90130-5

Sciunnach, D., and Garzanti, E. (2012). Subsidence history of the Tethys Himalaya. *Earth-Science Rev.* 111 (1-2), 179–198. doi:10.1016/j.earscirev.2011.11.007

Tamer, M., and Ketcham, R. (2020). Is low-temperature fission-track annealing in apatite a thermally controlled process? *Geochem. Geophys. Geosystems* 21 (3), e2019GC008877. doi:10.1029/2019GC008877

Vermeesch, P. (2009). RadialPlotter: A java application for fission track, luminescence and other radial plots. *Radiat. Meas.* 44 (4), 409–410. doi:10.1016/j.radmeas.2009.05.003

Wagner, G. A., and Reimer, G. M. (1972). Fission track tectonics: The tectonic interpretation of fission track apatite ages. *Earth Planet. Sci. Lett.* 14 (2), 263–268. doi:10.1016/0012-821X(72)90018-0

Wagner, G., and Van den Haute, P. (2012). *Fission-track dating*, 6. Germany: Springer Science & Business Media.

Wagner, T., Lee, J., Hacker, B. R., and Seward, G. (2010). Kinematics and vorticity in Kangmar Dome, southern Tibet: Testing midcrustal channel flow models for the Himalaya. *Tectonics* 29 (6). doi:10.1029/2010TC002746

Wang, S., Shen, X., Chevalier, M. L., Replumaz, A., Zheng, Y., Li, H., et al. (2022). Illite K-Ar and (U-Th)/He low-temperature thermochronology reveal onset timing of Yadong-Gulu rift in southern Tibetan Plateau. *Front. Earth Sci.* 10, 993796. doi:10.3389/feart.2022.993796

Wang, X., Zhang, J., Yan, S., and Liu, J. (2015). Structural characteristics and active time of the Kangmar detachment, Southern Tibet. *Geotect. Metallogenia* 39 (2), 250–259. (in Chinese with English abstract).

Wang, Y., Cai, K., Sun, M., Xiao, W., De Grave, J., Wan, B., et al. (2018). Tracking the multi-stage exhumation history of the Western Chinese tianshan by apatite fission track (AFT) dating: Implication for the preservation of epithermal deposits in the ancient orogenic belt. *Ore Geol. Rev.* 100, 111–132. doi:10.1016/j.oregeorev.2017.04.011

Wang, Y., Zeng, L., Gao, L. E., Chen, Z., and Li, S. (2022). Eocene thickening without extra heat in a collisional orogenic belt: A record from Eocene metamorphism in mafic dike swarms within the tethyan Himalaya, southern tibet. *Bulletin* 134 (5-6), 1217–1230. doi:10.1130/B35679.1

Wawrzyniec, T. F., Selverstone, J., and Axen, G. J. (2001). Styles of footwall uplift along the Simplon and Brenner normal fault systems, central and Eastern Alps. *Tectonics* 20 (5), 748–770. doi:10.1029/2000TC001253

Webb, A. A. G., Guo, H., Clift, P. D., Husson, L., Müller, T., Costantino, D., et al. (2017). The Himalaya in 3D: Slab dynamics controlled mountain building and monsoon intensification. *Lithosphere* 9 (4), 637–651. doi:10.1130/L636.1

Whipple, K. X., and Tucker, G. E. (1999). Dynamics of the stream-power river incision model: Implications for height limits of mountain ranges, landscape response timescales, and research needs. *J. Geophys. Res. Solid Earth* 104 (8), 17661–17674. doi:10.1029/1999JB900120

Xia, B., Xu, L. F., Zhang, Y. Q., Li, J., and Wang, Y. (2008). U-Pb SHRIMP zircon ages of the Kangmar granite in the southern Tibet. *J. Mineralogy Petrology* 28 (3), 72–76. (in Chinese with English abstract).

Xu, R. H., and Jin, C. W. (1986). A geochronological study in the middle of north Himalaya granite belt, Tibet. *Sci. Geol. Sin.* (in Chinese) 4, 339.

Yin, A., and Harrison, T. M. (2000). Geologic evolution of the Himalayan-Tibetan orogen. *Annu. Rev. earth Planet. Sci.* 28 (1), 211–280. doi:10.1146/annurev.earth.28.1.211

Zeng, L., Gao, L. E., Xie, K., and Liu-Zeng, J. (2011). Mid-Eocene high Sr/Y granites in the Northern Himalayan Gneiss Domes: Melting thickened lower continental crust. *Earth Planet. Sci. Lett.* 303 (3-4), 251–266. doi:10.1016/j.epsl.2011.01.005

Zeng, L., Liu, J., Gao, L., Xie, K., and Wen, L. (2009). Early Oligocene anatexis in the Yardoi gneiss dome, southern Tibet and geological implications. *Chin. Sci. Bull.* 54 (1), 104–112. doi:10.1007/s11434-008-0362-x

Zhang, H., Harris, N., Parrish, R., Kelley, S., Zhang, L., Rogers, N., et al. (2004). Causes and consequences of protracted melting of the mid-crust exposed in the North Himalayan antiform. *Earth Planet. Sci. Lett.* 228 (1-2), 195–212. doi:10.1016/j.epsl.2004.09.031

Zhang, J., Guo, L., and Zhang, B. (2007). Effect of replacing a hydroxyl group with a methyl group on arsenic (V) species adsorption on goethite (alpha-FeOOH). *Chin. J. Geol.* 42 (1), 16–21. doi:10.1016/j.jcis.2006.10.004

Zhang, J., Santosh, M., Wang, X., Guo, L., Yang, X., and Zhang, B. (2012). Tectonics of the northern Himalaya since the India–asia collision. *Gondwana Res.* 21 (4), 939–960. doi:10.1016/j.gr.2011.11.004

Zhao, W., Nelson, K. D., Che, J., Quo, J., Lu, D., Wu, C., et al. (1993). Deep seismic reflection evidence for continental underthrusting beneath southern Tibet. *Nature* 366 (6455), 557–559. doi:10.1038/366557a0

ZhangLiuRobertsLarrasoaa, Q. Q. A. P. J. C., and Jin, C. (2019). Mechanism for enhanced eolian dust flux recorded in NorthNorth Pacific ocean sediments since 4.0 ma: Aridity or humidity at dust source areas in the Asian interior? *Geology* 48 (1), 77–81. doi:10.1130/G46862.1